*Manuscript

Refinements in the characterisation of mode-mixity and small scale yielding at sharp notch roots

R.C. Flicek[a1] , D.A. Hills[a], and D. Dini[b]
[a]Department of Engineering Science, University of Oxford,
Parks Road, Oxford OX1 3PJ
[b]Department of Mechanical Engineering, Imperial College London,
South Kensington Campus, Exhibition Road, London SW7 2AZ

Abstract

This paper uses a modified formulation of Williams' asymptotic solution to examine the plastic zone near the root of sharp V-notches. A method for assessing whether the plastic zone is 'mode I like' or 'mode II like' or mixed-mode in character is presented. Small scale yielding limits are also calculated. This analysis is then applied to monotonic, mixed-mode experimental test data reported in the literature. The results indicate that: i) most tests were carried out within 5% small scale yielding and ii) the plastic zone of practical engineering components is likely to be either mainly mode I or mixed-mode in character.

Keywords: Complete contacts; asymptotic approaches; sharp notches; mode-mixity; Williams solution; small scale yielding

1. Introduction

Sharp notches, and features that are notch-like, such as adhered complete contacts and junctions between bonded components, give rise to implied elastic stress singularities, which then may prompt the nucleation of cracks, particularly under reversing loads. The amount of theoretical work on the subject is enormous, and much of it is very elegant with great mathematical finesse (see e.g. [1, 2, 3, 4, 5, 6, 7, 8, 9] and [10] for a review). Here, the analysis is down to earth but intended to provide comprehensive information – meaning for a wide range of notch angles – about the nature of the notch root region in which the process zone lies, i.e. the region within the plastic zone where irreversibilities leading to crack nucleation occur. The intention is

[1]Corresponding author: R.C. Flicek. Email: robert.flicek@eng.ox.ac.uk.

to provide three developments: i) to construct an alternative way of defining when the plastic and hence process zone is 'mode I like' or 'mode II like' or mixed-mode in nature, refining the ideas developed in [11] but based on a full-field correlation; ii) to provide an improved way of displaying the results of this calculation that enables the results of experimental work to be classified easily, and which is readily extendable to any notch angle; and iii) to show, on the same diagram, the conditions under which small scale yielding requirements are also satisfied. We are specifically interested in the challenging case where both eigensolutions are singular, i.e. when the notch angle is greater than 257.4°.

2. Formulation

The previous paper [11] hinges on a new way of displaying Williams' solution [12] for the state of stress at the tip of a sharp, semi-infinite elastic notch, such as that shown in Figure 1. Williams' solution may be interpreted as giving the stress state in finite problems incorporating a notch of interior angle 2α as

$$\sigma_{ij}(r,\theta) = K_I r^{\lambda_I - 1} f_{ij}^I(\theta) + K_{II} r^{\lambda_{II} - 1} f_{ij}^{II}(\theta) + \text{bounded terms}, \tag{1}$$

where $i,j \in \{r,\theta\}$, and (r,θ) is the polar coordinate set defined in Figure 1. If we assume plane strain, then

$$\sigma_{zz} = \nu(\sigma_{rr} + \sigma_{\theta\theta}), \tag{2}$$

where ν is Poisson's ratio. In equation (1), the terms λ_n, where $n \in \{I, II\}$, are the eigenvalues of the system, which are given by the lowest roots of the following equations

$$\lambda_I \sin(2\alpha) + \sin(2\alpha\lambda_I) = 0 \tag{3a}$$

$$\lambda_{II} \sin(2\alpha) - \sin(2\alpha\lambda_{II}) = 0, \tag{3b}$$

and these are plotted in Figure 2. The terms $f_{ij}^n(\theta)$ are the angular eigenfunctions, which we have normalised so that $f_{\theta\theta}^I(0) = 1$ and $f_{r\theta}^{II}(0) = 1$, and these are written out explicitly in Appendix Appendix A. We note that both the eigenvalues and the angular eigenfunctions are fully determined by the notch angle, 2α, and are independent of the finite geometry under consideration. The terms K_n are the *generalised stress intensity factors* (also sometimes referred to as *notch stress intensity factors*), and these must be calibrated from the finite problem under consideration. The angular eigenfunctions of the mode I, II solutions uncouple along the notch bisector, i.e. $f_{r\theta}^I(0) = 0$

and $f_{\theta\theta}^{II}(0) = 0$, and thus we can define the generalised stress intensity factors as

$$K_I = \lim_{r\to 0} \sigma_{\theta\theta}(r,0) r^{1-\lambda_I} \tag{4a}$$

$$K_{II} = \lim_{r\to 0} \sigma_{r\theta}(r,0) r^{1-\lambda_{II}}. \tag{4b}$$

We note that equations (3a),(4a) correspond to the symmetric term of the solution, whereas equations (3b),(4b) correspond to the anti-symmetric term.

2.1. Alternative method of display

From Figure 2, we can see that within the range $180° < 2\alpha \leq 360°$ there are three distinct forms that the semi-infinite solution can take. The extreme case when $2\alpha = 360°$ corresponds to the familiar problem from fracture mechanics of an edge crack. Here, of course, both eigensolutions are square root singular, and thus the mode-mixity of the stress field is self similar with r. In contrast, within the range $180° < 2\alpha < 257.4°$, we see that only the mode I eigensolution is singular, so this term will dominate the characteristic of the state of stress whenever the notch root is approached.

We are most interested, however, in notch angles within the range $257.4° < 2\alpha < 360°$ for which both eigensolutions are singular but are of different strengths, i.e. $1/2 < \lambda_I < \lambda_{II} < 1$. Within this range, it is clear that the more strongly singular mode I solution will always dominate the characteristic of the state of stress as an observation point approaches the notch root (unless the remote load is purely mode II in character). In contrast, 'remote' from the notch root, the less strongly singular mode II solution will dominate. Thus, we see that there is a length scale associated with Williams' (semi-infinite) solution itself, and this can be brought out more clearly by abstracting an alternative set of parameters from the generalised stress intensity factors as in [11]

$$G_0 = |K_I|^{\frac{\lambda_{II}-1}{\lambda_{II}-\lambda_I}} |K_{II}|^{\frac{\lambda_I-1}{\lambda_I-\lambda_{II}}} \tag{5a}$$

$$d_0 = \left|\frac{K_{II}}{K_I}\right|^{\frac{1}{\lambda_I-\lambda_{II}}}. \tag{5b}$$

Williams' solution can then be re-written as[2]

$$\frac{\sigma_{ij}(r,\theta)}{G_0} = \left(\frac{r}{d_0}\right)^{\lambda_I - 1} f_{ij}^{I}(\theta) + \left(\frac{r}{d_0}\right)^{\lambda_{II} - 1} f_{ij}^{II}(\theta). \tag{6}$$

When written in this form, it is clear that d_0 represents, in some sense, the boundary between mode I dominant behaviour (if $r \ll d_0$) and mode II dominant behaviour (if $r \gg d_0$), whilst G_0 serves to regulate the magnitude of the state of stress as a whole.

This was the state of refinement that was used in our previous paper [11], and we now propose further changes to bring out several issues clearly. To do this, we imagine that a calibration has been found for the generalised stress intensity factors in whatever configuration is being studied. From dimensional considerations, we see that any set of calibrations can be written in the form

$$K_n = mka^{1-\lambda_n} S_n, \tag{7}$$

where a is a characteristic length scale of the finite problem (e.g. the distance to the nearest geometric feature, see Figure 9 for examples), k is the yield stress of the material in pure shear, and m is a dimensionless scalar that scales the applied load. This enables us to determine a dimensionless calibration of the mode n generalised stress intensity factor, denoted S_n. The parameters G_0 and d_0 may be written in terms of dimensionless generalised stress intensity factors as

$$\frac{G_0}{k} = |mS_I|^{\frac{\lambda_{II}-1}{\lambda_{II}-\lambda_I}} \, |mS_{II}|^{\frac{\lambda_I - 1}{\lambda_I - \lambda_{II}}} \tag{8a}$$

$$\frac{d_0}{a} = \left|\frac{S_{II}}{S_I}\right|^{\frac{1}{\lambda_I - \lambda_{II}}}. \tag{8b}$$

Once defined in this way, it is clear that d_0 is independent of the magnitude of the applied load, m, whereas G_0 is a function of m. Furthermore, as d_0 is solely dependent on the ratio of the generalised stress intensity factors, we see that it provides a measure of the mode-mixity associated with the given loading configuration. However, as we shall soon see, the mode-mixity in the region relevant to crack nucleation is, in some cases, quite different from the *nominal* mode-mixity of the loading configuration.

[2]Note that if the remote loads result in pure mode I or pure mode II conditions, this alternative formulation cannot be used because d_0 and G_0 will tend either to zero or to infinity. However, so long as there is some contribution from both terms in the solution (even if one mode dominates the stress field), this formulation remains valid. We also note that numerical difficulties arise when $\lambda_I \sim \lambda_{II}$, i.e. for $2\alpha \gtrsim 330^\circ$ (see Fiure 2), due to the definition of d_0, G_0.

3. Mode-mixity at the process zone

We may think of the process zone at the notch root, $r_p(\theta)$, as a region within the plastic zone where irreversibilities lead to crack nucleation. Its properties are determined by the plastic hinterland, i.e. the region where the yield criterion is violated, as is customary in estimates of small scale yielding plastic zones. An idealised diagram of the process zone, $r_p(\theta)$, which shows both plastic lobes, $r_{p1}(\theta), r_{p2}(\theta)$, is displayed in Figure 1.

The size of the process zone is, of course, controlled by the ratio of the magnitude of the applied load, G_0, to the strength of the material, k. Thus when $G_0 \ll k$, the process zone will be small in comparison to d_0, i.e. $r_p \ll d_0$, and will be mainly mode I in character. As G_0 is increased, the process zone will both rotate and increase in size, first becoming mixed-mode in character when $r_p \sim d_0$, and finally becoming mode II in character when $r_p \gg d_0$. Hence we see that this ratio, G_0/k, determines the mode-mixity *at the scale of the process zone*. In the earlier paper [11], we characterised the process zone as being mainly mode I or mainly mode II simply by looking at the orientation of the plastic lobes. Here we use a different approach, based on a local full field collocation with, as reference, pure mode I and pure mode II process zones, $r_p^I(\theta), r_p^{II}(\theta)$.

The second invariant of deviatoric stress in terms of the non-zero stress components arising here is

$$J_2 = \sigma_{rr}^2 + \sigma_{\theta\theta}^2 + \sigma_{zz}^2 - (\sigma_{rr}\sigma_{\theta\theta} + \sigma_{\theta\theta}\sigma_{zz} + \sigma_{zz}\sigma_{rr}) + 3\sigma_{r\theta}^2, \tag{9}$$

and with this scaling von Mises yield criterion is

$$J_2 = 3k^2. \tag{10}$$

The *size and shape* of the mixed-mode process zone, $r_p(\theta)$, can be obtained *within the asymptote* by equating expressions (9),(10) and substituting in stresses from equations (2),(6). Similarly, we obtain the *shape* of the pure mode n process zones, $r_p^n(\theta)$, by substituting stresses of the form

$$\sigma_{ij}^n(r,\theta) = K_n r^{\lambda_n - 1} f_{ij}^n(\theta) = (mka^{1-\lambda_n} S_n) r^{\lambda_n - 1} f_{ij}^n(\theta) \tag{11}$$

into equation (9), using equation (2), and equating the resulting expression with equation (10).

Notice that we can determine both the shape and the size of the mixed-mode process zone within the asymptote because it contains an intrinsic length scale, d_0. In contrast, the pure mode I, II process zones are self-similar and contain no intrinsic length scale, so we cannot determine their size without normalising the solution by the characteristic length from a finite problem, a.

3.1. Comparison of pure and mixed-mode process zones

We now wish to compare the *shape* (but not the size) of the mixed-mode process zone with the pure mode I, II process zones. For this purpose, we use the *correlation coefficient*, ρ, (also referred to as *Pearson's product-moment correlation coefficient*) because it is invariant with both scale and origin. We denote the correlation coefficient of the full field process zone, $r_p(\theta)$, with respect to the pure mode n process zone as ρ_n. The correlation coefficient is calculated by dividing the covariance of two curves by the product of their standard deviations. We note that, $-1 \leq \rho \leq 1$, where $\rho = 1$ implies a perfect positive linear relationship, $\rho = -1$ implies a perfect negative linear relationship, and $\rho = 0$ implies no linear relationship.

It is probably easiest to visualise the calculation of the correlation coefficients, ρ_I, ρ_{II}, on a Cartesian plot of $r_p(\theta)$ vs. θ. An example of this is shown in Figure 3 for a 270° notch with $\nu = 0.3$. In this figure, we plot the *shape* of: (a) a pure mode I process zone and a mixed-mode process zone of $G_0/k = 0.2495$ and (b) a pure mode II process zone and a mixed-mode process zone of $G_0/k = 1.292$. Each process zone in this figure is normalised by its maximum value because the relative size of the process zones has no influence on the correlation coefficient. We note that the correlation coefficients between the process zones shown in Figure 3(a),(b) are $\rho_I = 0.7, \rho_{II} = 0.7$, respectively. See Appendix Appendix B for some more details on how we carry out this calculation.

In order to illustrate more clearly the relationship between the correlation coefficients and the strength of the applied load, we plot ρ_I, ρ_{II} (when positive) over a wide range of G_0/k in Figure 4 for the example case of a 270° notch with $\nu = 0.3$. In this figure, we see that for very small G_0/k (when $r_p \ll d_0$) the correlation with a pure mode I process zone is high (and the correlation with a pure mode II process zone is negative and not shown). However, as G_0/k is increased, ρ_I decreases until it reaches zero (when $r_p \sim d_0$) and the correlation with the mode II process zone becomes positive. As G_0/k is increased further, ρ_{II} increases and eventually approaches unity (when $r_p \gg d_0$).

3.2. Mode-mixity results

We now wish to use this technique to characterise the mode-mixity of the process zone and to obtain general results, which can be used to characterise experimental data. To do this, we select values of ρ_I, ρ_{II} that mark the boundary between a mixed-mode process zone and a process zone that is 'mainly mode I' or 'mainly mode II' in character. In Figure 4, we show, as an example, the regions that result if we assume $\rho_I, \rho_{II} > 0.7$ to constitute a process zone that is mode I or mode II dominated.

Notice from Figure 4 that any value of G_0/k corresponds to fixed values of ρ_I, ρ_{II} and thus to fixed levels of mode-mixity at the process zone. We exploit this in Figure 5 and show the values of G_0/k for which the process zone is mode I dominated, mode II dominated, or mixed-mode in character for notch angles within the range $270^\circ < 2\alpha < 330^\circ$ for $\nu = 0.3$. Because the values of ρ_I, ρ_{II} assumed to constitute a process zone that is mode I or mode II dominated is arbitrary, we show results corresponding to four choices of ρ_I, ρ_{II}, viz. $0.95, 0.9, 0.8, 0.7$.

Although Figure 5 is useful and comprehensive, it employs an unfamiliar characterisation of the magnitude of the load, G_0/k, which the user will have to calculate from equation (5a) or (8a). Alternatively, the regions of mode I, II domination of the process zone can be plotted in generalised stress intensity space, i.e. on a plot of mS_{II} vs. mS_I (or equivalently $K_{II}a^{\lambda_{II}-1}/k$ vs. $K_I a^{\lambda_I - 1}/k$), and this is done in Figure 6. In Figure 6(a), we plot results corresponding to $\rho_I, \rho_{II} = 0.95, 0.9, 0.8, 0.7$ but only for a particular notch angle, $2\alpha = 270^\circ$, with $\nu = 0.3$. In Figure 6(b), we show results corresponding only to $\rho_I, \rho_{II} = 0.9$ but for three notch angles, viz. $2\alpha = 270^\circ, 300^\circ, 330^\circ$, again with $\nu = 0.3$. We note that to plot the results in Figure 6, we simply substitute the value of G_0/k corresponding to ρ_I, ρ_{II} from Figure 5 into equation (8a).

From Figures 5,6(a), we see that the selection of ρ_I, ρ_{II} has a very significant effect on the size of the regions in which the process zone may be said to be mode I or mode II dominated. This is, of course, because ρ_I, ρ_{II} control the definition of what constitutes a process zone that is mode I or mode II dominated. From Figure 6(a), we also see that the effect of varying ρ_I, ρ_{II} is to apply a simple dilation to these boundaries.

In contrast, in Figure 6(b), we see that varying the notch angle, 2α, has marked effects not only on the size but also on the shape of the mode I and mode II dominated regions. In fact, it is clear that varying the notch angle significantly alters the relative sizes of the mode I and mode II dominated regions. This is not surprising and is explained by the variation of the strength of the mode I and mode II singularities with notch angle (see Figure 2). Thus, we see that for 'small' notch angles the mode I dominated region is much larger than the mode II dominated region because the mode I singularity is much stronger than the mode II singularity, e.g. for a 270° notch $\lambda_I - 1 = -0.4555$ and $\lambda_{II} - 1 = -0.0915$. On the other hand, the mode I and mode II dominated regions are of a similar size for larger notch angles because the singularities are of similar strengths, e.g. for a 330° notch $\lambda_I - 1 = -0.4985$ and $\lambda_{II} - 1 = -0.4018$.

4. Small scale yielding limits

We now extend the scope of the calculation to permit the bound on the load needed to maintain small scale yielding conditions to be calculated and displayed in plots of mS_{II} vs. mS_I. This calculation is very similar to the familiar approach in fracture mechanics for calculating small scale yielding limits. We simply note that this asymptotic solution is valid only very near to the sharp corner where the singular solution dominates the state of stress, i.e. for $r \ll a$. Hence, this solution can only be used to describe the process zone when $r_p^{\max}/a \ll 1$, where $r_p^{\max}$ is the maximum extent of the plastic zone.

We now use the same basic formulation described in detail above but include information about the distance to the nearest salient geometric feature, a, by normalising the solution by this parameter. We obtain an estimate of the size of the process zone by substituting stresses from equations (1),(2) into equation (9) and using equations (7),(10). We then calculate the combinations of mS_I, mS_{II} that result in $r_p^{\max}/a$ being equal to the desired small scale yielding limit. See Appendix Appendix C for some more details on this calculation.

As can be seen in Figure 1, the process zone has two lobes, $r_{p1}(\theta), r_{p2}(\theta)$. In Figure 7, we show the values of mS_I, mS_{II} that result in $r_{p1}^{\max}/a, r_{p2}^{\max}/a = 0.1$ for the example case of $2\alpha = 270^\circ$ with $\nu = 0.3$. The shaded area in this figure gives the range of mS_I, mS_{II} for which both plastic lobes, $r_{p1}^{\max}, r_{p2}^{\max}$, are within small scale yielding. Hence in all subsequent plots, we show only the curve corresponding to the edge of this shaded region.

4.1. Small scale yielding results

We now wish to create general plots that can be superposed with the mode-mixity results shown in Figure 6(a) and used to classify experimental data. Of course, the selection of the small scale yielding limit, $r_p^{\max}/a$, is also arbitrary and depends on how much influence of the (neglected) higher order terms in the series expansion may be accepted. Thus, we show results for several small scale yielding limits, viz. $r_p^{\max}/a = 0.01, 0.05, 0.1, 0.15$, in Figure 8(a) for the example case of $2\alpha = 270^\circ$ with $\nu = 0.3$. In Figure 8(b), we show only one small scale yielding limit, $r_p^{\max}/a = 0.1$, but for three notch angles, viz. $2\alpha = 270^\circ, 300^\circ, 330^\circ$ again with $\nu = 0.3$.

As is no surprise, Figure 8(a) illustrates that the selection of the small scale yielding limit, $r_p^{\max}/a$, has a significant effect on the range of loads, i.e. mS_I, mS_{II}, that fall within small scale yielding. It is also apparent that the effect of increasing $r_p^{\max}/a$ is to apply a fairly uniform dilation the small scale yielding curve.

In contrast, and notably, we see from Figure 8(b) that varying the notch angle has only the most minuscule effect on the area within small scale yielding for loadings that are mainly mode I in character (i.e. that are very near to the mS_I axis) but a marked effect for loadings that are mainly mode II in character (i.e. very near to the mS_{II} axis). We attribute this to the fact that the order of the mode II singularity changes much more rapidly with notch angle than does the mode I singularity (see Figure 2).

5. Example application

We now wish to apply these techniques to analyse experimental data reported in the literature. A review of the literature reveals that a great deal of experiments have been carried out to validate the various brittle fracture criteria that have been proposed for sharp and blunt notches, e.g. [13, 14, 15, 16, 17, 18, 19, 20, 21]. Of the various experiments reported, we have selected five groups of tests, viz. [22, 23, 16, 24, 17], which were performed with polymethyl metacrylate (PMMA) under mixed-mode, monotonic loading conditions.

Idealised diagrams (not to scale) of the various test geometries we have selected are shown in Figure 9. In this figure, the applied loads denoted P, T, M correspond to an applied normal traction, shear traction, distributed moment, respectively, and $R1, R2$ are reaction forces that arise at supports in the test rig. We also show the dimension we have selected as the characteristic length, a, which controls the definition of the small scale yielding limit and also affects the values computed for the dimensionless generalised stress intensity factors, S_n. As can be seen in the figure, we have chosen a to be the smaller of: i) half the distance to the nearest sharp re-entrant corner ($2\alpha > 180°$) or ii) the full distance to any other geometric feature. We have selected a in this way because sharp re-entrant corners sustain a very large stress intensification and thus have an early influence on the stress state, whereas external corners ($2\alpha < 180°$) and smooth surfaces do not.

To apply our analysis, we require knowledge of the generalised stress intensity factors at failure, which we obtained from [22, 14, 23, 16, 24, 17]. The details of how we processed these data is given in Appendix Appendix D. For our analysis, we also require knowledge of Poisson's ratio, ν, and this is quoted as 0.35 in [14], 0.36 in [23, 16, 24], and 0.38 in [17]. In Figure 10, we show (a) the mode-mixity results for $\rho_I, \rho_{II} = 0.9$ and (b) the small scale yielding results for $r_p^{\max}/a = 0.1$ over a wide range of values of Poisson's ratio, viz. $\nu = 0.1, 0.3, 0.5$, for the example case of a 270° notch. This figure makes clear that the effect of varying ν from 0.35 to 0.38 is negligible, so all subsequent results are computed for $\nu = 0.36$.

In Figure 11, we plot the generalised stress intensity factors at failure on plots of mS_{II} vs. mS_I. These plots show the regions in which the process zone is mode I dominated, mode II dominated, or is mixed-mode in character according to four definitions, viz. $\rho_I, \rho_{II} = 0.95, 0.9, 0.8, 0.7$.[3] Small scale yielding limits of $r_p^{\max}/a = 0.01, 0.05, 0.1, 0.15$ are also shown simultaneously. In Figure 12, we display all the data[4] presented in Figure 11 on a single plot of G_0/k vs. 2α that shows the mode-mixity of the process zone again for $\rho_I, \rho_{II} = 0.95, 0.9, 0.8, 0.7$. The benefit of this plot is that data from many different notch angles can be plotted simultaneously, but this comes at the cost of being unable to view small scale yielding information.

5.1. Small scale yielding of experimental data

From Figure 11, we see that much of the data are within 1% small scale yielding ($r_p^{\max}/a = 0.01$), including all of the tests by Seweryn et al. [22] and Priel et al. [16] and also most of those by Dunn et al. [23], Kim and Cho [24], and Ayatollahi et al. [17]. The remainder of the tests by Dunn et al. [23] are within 5% small scale yielding. This is also true of most of the tests by Kim and Cho [24] and Ayatollahi et al. [17] aside from those conducted under mode II dominated loading on notches of $2\alpha \lesssim 300^\circ$ (see Figures 11(a),(c),(d)). In Figure 11(a), we see that for mode II dominated loading the tests by Kim and Cho [24] are between 5% and 15% small scale yielding, whereas those by Ayatollahi et al. [17] are outside 15% small scale yielding. Here, it is clear that the the small scale yielding assumption is being stretched, and this is likely because the stress field is only very weakly singular ($\lambda_{II} - 1 = -0.0915$).

That some of the tests stretch the small scale yielding assumption may be evidenced in [24] by the observed critical loads exceeding the predictions of the brittle fracture criterion used by the authors, which is based on an asymptotic analysis. However, Kim and Cho [24] only remark on the general underestimation of failure loads (for all notch angles) and attribute this to the effect of a small but finite notch root radius. In contrast, the analysis by Ayatollahi et al. [17] predicts failure accurately even in pure mode II conditions for $2\alpha = 270^\circ$ when our analysis suggests that the process zone is outside 15% small scale yielding. Although this is somewhat surprising, similar findings were also reported by Dunn et al. [23]. This seems to imply

[3]The only exception to this is in Figure 11(g) for $2\alpha = 330^\circ$ for which only the results for $\rho_{II} = 0.95, 0.9, 0.8, 0.7$ and $\rho_I = 0.9, 0.8, 0.7$ are shown because the $\rho_I = 0.95$ case failed to converge.

[4]We note that this plot excludes data obtained in pure I, II loading conditions because under these conditions d_0, G_0 are not defined.

the useful result that the asymptotic solution can be used to predict crack initiation even as higher order terms begin to exert an influence on the process zone.

5.2. Mode-mixity of experimental data

From Figures 11(a),11(e),12, we see that all the data reported by Dunn et al. [23] and the majority of those by Priel et al. [16] resulted in a process zone that was mainly mode I in character. In fact, Figure 11(a),12 shows that the tests by Dunn et al. [23] resulted in a process zone with a correlation coefficient of between $0.8 < \rho_I < 0.9$ with a pure mode I process zone. This is in agreement with the findings of Dunn et al. [23] as they were able to predict failure accurately based on a critical mode I generalised stress intensity alone. As can be seen in Figure 11(e), the tests carried out by Priel et al. [16] extend over a wider range of mode-mixities than the tests in [23] but still are only mildly mixed-mode in character at the level of the process zone. This finding is in agreement with the analysis of Priel et al. [16] as well as with remarks made by Ayatollahi et al. [17] in their analysis of a subset of the data in [16].

The data reported by Seweryn et al. [22], Ayatollahi et al. [17] and Kim and Cho [24] explore the full range of mode-mixities. However, for small notch angles ($2\alpha \lesssim 300^\circ$), we see that these nominally mixed-mode loading conditions usually result in a process zone that is mainly mode I or only mildly mixed-mode in character. In fact, for these notch angles, the process zone is almost never found to be mainly mode II in character aside from pure mode II loading conditions. Thus, for practical engineering components, we see that the process zone will often be mainly mode I in character. This is, of course, due to the difference in the order of the mode I, II singularities (see Figure 2), and so we temper these remarks because as $2\alpha \to 360^\circ$ this difference decreases. Hence, for larger notch angles, mixed-mode conditions at the process zone become increasingly likely and mainly mode II conditions become increasingly plausible.

6. Conclusion

We have taken further steps beyond that described in [11] to include useful information in a simple portryal of the results of the Williams eigensolution calculation when applied to notch experiments. Specifically, two quantities are mapped out, viz. i) the proximity of the qualities of the process zone to both mode I and mode II behaviour, and ii) the maximum load that may be tolerated without violating small-scale yielding considerations. The form chosen is particularly well suited to categorising the results of any experimental investigation because it is easy to see the underlying quality of

the plastic and hence process zone. This can also be used in combination with, for example, strain energy density and/or finite distance and volume averaging methods to assess the likelihood of brittle failures in notched components [16, 18, 19, 20]. Higher order terms could also be embedded [24, 25].

Application of this analysis to mixed-mode fracture data reported in the literature shows that the majority of tests were conducted within 5% small scale yielding ($r_p^{\max}/a = 0.05$). The only exception to this was for oblique notches subjected to mode II dominated loading conditions for which the singularity of the stress field is relatively weak. The results also indicate that mode II domination of the stress field is very unlikely to occur for oblique notch angles, and hence in practice; indeed, in many cases, the process zone will be mainly mode I in character – even under nominally mixed-mode remote loading. The exception is for very acute notch angles for which mixed-mode conditions are most likely and mainly mode II conditions are conceivable.

Acknowledgement

R. C. Flicek would like to thank Rolls-Royce plc and the Technology Strategy Board for financial support under the programme SILOET-II. The authors wish to thank Rolls-Royce plc for granting permission to publish this work.

References

[1] V. G. Maz'ya, S. A. Nazarov, and V. A. Plamenevskii. Evaluation of the asymptotic form of the "intensity coefficients" on approaching corner or conical points. *USSR Comput. Math. Math+*, 23(2):50–83, 1983. doi: 10.1016/S0041-5553(83)80047-0.

[2] P. Grisvard. *Boundary value problems in non-smooth domains*. Pitman, London, 1985.

[3] D. Leguillon and E. Sanchez-Palencia. *Computation of singular solutions in elliptic problems and elasticity*. Recherches en mathématiques appliquées, Wiley, 1987.

[4] M. Costabel and M. Dauge. General edge asymptotics of solutions of second-order elliptic boundary value problems I. *P. Roy. Soc. Edinb. A.*, 123(1):109–155, 1993. doi: 10.1017/S0308210500021272.

[5] M. Costabel and M. Dauge. General edge asymptotics of solutions of second-order elliptic boundary value problems II. *P. Roy. Soc. Edinb. A.*, 123(1):157–184, 1993. doi: 10.1017/S0308210500021284.

[6] P. Lazzarin and R. Tovo. A unified approach to the evaluation of linear elastic stress fields in the neighborhood of cracks and notches. *Int. J. Fracture.*, 78(1):3–19, 1996. doi: 10.1007/BF00018497.

[7] G. B. Sinclair. Stress singularities in classical elasticity-I: removal, interpretation, and analysis. *Appl. Mech. Rev. 57 (4)*, 57(4):251–297, 2004. doi: 10.1115/1.1762503.

[8] G. B. Sinclair. Stress singularities in classical elasticity-II: asymptotic identification. *Appl. Mech. Rev. 57 (5)*, 57(5):385–439, 2004. doi: 10.1115/1.1767846.

[9] A. Carpinteri, P. Cornetti, N. Pugno, A. Sapora, and D. Taylor. A finite fracture mechanics approach to structures with sharp V-notches. *Eng. Fract. Mech.*, 75(7):1736–1752, 2008. doi: 10.1016/j.engfracmech.2007.04.010.

[10] A. Carpinteri and M. Paggi. Asymptotic analysis in linear elasticity: From the pioneering studies by wieghardt and irwin until today. *Eng. Fract. Mech.*, 76(12):1771 – 1784, 2009. doi: 10.1016/j.engfracmech.2009.03.012.

[11] D. A. Hills and D. Dini. Characteristics of the process zone at sharp notch roots. *Int. J. Solids. Struct.*, 48(14-15):2177–2183, 2011. doi: 10.1016/j.ijsolstr.2011.03.023.

[12] M. L. Williams. Stress singularities resulting from various boundary conditions in angular plates in extension. *J. Appl. Mech.*, 19:526–528, 1952.

[13] A. Seweryn. Brittle fracture criterion for structures with sharp notches. *Eng. Fract. Mech. 47 (5)*, 47(5):673–681, 1994. doi: 10.1016/0013-7944(94)90158-9.

[14] A. Seweryn and A. Łukaszewicz. Verification of brittle fracture criteria for elements with V-shaped notches. *Eng. Fract. Mech.*, 69(13):1487–1510, 2002. doi: 10.1016/S0013-7944(01)00138-2.

[15] M. L. Dunn, W. Suwito, and S. Cunningham. Fracture initiation at sharp notches: correlation using critical stress intensities. *Int. J. Solids. Struct.*, 34(29):3873–3883, 1997. doi: 10.1016/S0020-7683(96)00236-3.

[16] E. Priel, A. Bussiba, I. Gilad, and Z. Yosibash. Mixed mode failure criteria for brittle elastic V-notched structures. *Int. J. Fracture.*, 144 (4):247–265, 2007. doi: 10.1007/s10704-007-9098-x.

[17] M. R. Ayatollahi, A. R. Torabi, and P. Azizi. Experimental and theoretical assessment of brittle fracture in engineering components containing a sharp V-notch. *Exp. Mech.*, 51(6):919–932, 2011. doi: 10.1007/s11340-010-9401-z.

[18] M. Elices, G. V. Guinea, J. Gomez, and J. Planas. The cohesive zone model: advantages, limitations and challenges. *Eng. Fract. Mech.*, 69 (2):137–163, 2002. doi: 10.1016/S0013-7944(01)00083-2.

[19] P. Lazzarin and R. Zambardi. A finite-volume-energy based approach to predict the static and fatigue behavior of components with sharp V-shaped notches. *Int. J. Fracture.*, 112(3):275–298, 2001. doi: 10.1023/A:1013595930617.

[20] P. Lazzarin, F. Berto, M. Elices, and J. Gómez. Brittle failures from U-and V-notches in mode I and mixed, I+ II, mode: a synthesis based on the strain energy density averaged on finite-size volumes. *Fatigue Fract. Eng. Mater. Struct.*, 32(8):671–684, 2009. doi: 10.1111/j.1460-2695.2009.01373.x.

[21] D. Leguillon. Strength or toughness? A criterion for crack onset at a notch. *Eur. J. Mech. A-Solid*, 21(1):61–72, 2002. doi: 10.1016/S0997-7538(01)01184-6.

[22] A. Seweryn, S. Poskrobko, and Z. Mróz. Brittle fracture in plane elements with sharp notches under mixed-mode loading. *J. Eng. Mech.*, 123(6):535–543, 1997. doi: 10.1061/(ASCE)0733-9399(1997)123:6(535).

[23] M. L. Dunn, W. Suwito, S. Cunningham, and C. W. May. Fracture initiation at sharp notches under mode I, mode II, and mild mixed mode loading. *Int. J. Fracture.*, 84(4):367–381, 1997. doi: 10.1023/A:1007346203407.

[24] J. K. Kim and S. B. Cho. A unified brittle fracture criterion for structures with sharp V-notches under mixed mode loading. *J. Mech. Sci. Technol.*, 22(7):1269–1278, 2008. doi: 10.1007/s12206-008-0315-y.

[25] C. Z. Cheng, Z. R. Niu, and N. Recho. Effect of non-singular stress on the brittle fracture of V-notched structure. *Int. J. Fracture.*, 174(2): 127–138, 2012. doi: 10.1007/s10704-012-9680-8.

[26] W. Suwito, M. L. Dunn, and S. J. Cunningham. Fracture initiation at sharp notches in single crystal silicon. *J. Appl. Phys.*, 83(7):3574–3582, 1998. doi: 10.1063/1.366574.

[27] W. Suwito, M. L. Dunn, S. J. Cunningham, and D. T. Read. Elastic moduli, strength, and fracture initiation at sharp notches in etched single crystal silicon microstructures. *J. Appl. Phys.*, 85(7):3519–3534, 1999. doi: 10.1063/1.369711.

[28] A. Seweryn and K. Molski. Elastic stress singularities and corresponding generalized stress intensity factors for angular corners under various boundary conditions. *Eng. Fract. Mech.*, 55(4):529–556, 1996. doi: 10.1016/S0013-7944(96)00035-5.

Appendix A. Williams' solution angular eigenfunctions

The angular eigenfunctions, $f_{ij}^{n}(\theta)$, with the normalisation we have used in our formulation of Williams' solution are given by [11]

$$f_{rr}^{I}(\theta) = \frac{\cos[(\lambda_I - 1)\alpha]\cos[(\lambda_I + 1)\theta] - \frac{\lambda_I - 3}{\lambda_I + 1}\cos[(\lambda_I + 1)\alpha]\cos[(\lambda_I - 1)\theta]}{\cos[(\lambda_I + 1)\alpha] - \cos[(\lambda_I - 1)\alpha]} \tag{A.1a}$$

$$f_{\theta\theta}^{I}(\theta) = \frac{\cos[(\lambda_I - 1)\alpha]\cos[(\lambda_I + 1)\theta] - \cos[(\lambda_I + 1)\alpha]\cos[(\lambda_I - 1)\theta]}{\cos[(\lambda_I - 1)\alpha] - \cos[(\lambda_I + 1)\alpha]} \tag{A.1b}$$

$$f_{r\theta}^{I}(\theta) = \frac{\sin[(\lambda_I - 1)\alpha]\sin[(\lambda_I + 1)\theta] - \sin[(\lambda_I + 1)\alpha]\sin[(\lambda_I - 1)\theta]}{\sin[(\lambda_I - 1)\alpha] - \frac{\lambda_I + 1}{\lambda_I - 1}\sin[(\lambda_I + 1)\alpha]} \tag{A.1c}$$

$$f_{rr}^{II}(\theta) = \frac{\sin[(\lambda_{II} - 1)\alpha]\sin[(\lambda_{II} + 1)\theta] - \frac{\lambda_{II} - 3}{\lambda_{II} + 1}\sin[(\lambda_{II} + 1)\alpha]\sin[(\lambda_{II} - 1)\theta]}{\sin[(\lambda_{II} - 1)\alpha] - \frac{\lambda_{II} - 1}{\lambda_{II} + 1}\sin[(\lambda_{II} + 1)\alpha]} \tag{A.2a}$$

$$f_{\theta\theta}^{II}(\theta) = \frac{\sin[(\lambda_{II} - 1)\alpha]\sin[(\lambda_{II} + 1)\theta] - \sin[(\lambda_{II} + 1)\alpha]\sin[(\lambda_{II} - 1)\theta]}{-\sin[(\lambda_{II} - 1)\alpha] + \frac{\lambda_{II} - 1}{\lambda_{II} + 1}\sin[(\lambda_{II} + 1)\alpha]} \tag{A.2b}$$

$$f_{r\theta}^{II}(\theta) = \frac{\cos[(\lambda_{II} - 1)\alpha]\cos[(\lambda_{II} + 1)\theta] - \cos[(\lambda_{II} + 1)\alpha]\cos[(\lambda_{II} - 1)\theta]}{\cos[(\lambda_{II} - 1)\alpha] - \cos[(\lambda_{II} + 1)\alpha]}. \tag{A.2c}$$

Appendix B. Mode-mixity calculation

To approximate the process zone of a notch subjected to mixed-mode loading, $r_p(\theta)$, we equate expressions (9),(10), substitute in stresses from equations (2),(6), and manipulate and simplify the resulting expression to give

$$3\left(\frac{k}{G_0}\right)^2 = \left(\frac{r_p}{d_0}\right)^{2(\lambda_I-1)} p_I(\theta) + \left(\frac{r_p}{d_0}\right)^{2(\lambda_{II}-1)} p_{II}(\theta) + \left(\frac{r_p}{d_0}\right)^{(\lambda_I+\lambda_{II}-2)} p_M(\theta). \tag{B.1}$$

We see that the left side of this equation accounts for the strength of the applied load, and the right side specifies the size and shape of the process zone based on the contribution of three terms, viz. pure mode I, pure mode II, and mixed-mode. The $p_\xi(\theta)$ functions in this expression, where $\xi \in \{I, II, M\}$, account for the θ-variation of the mode I, mode II, and mixed-mode term, respectively. Note that the $p_\xi(\theta)$ functions are comprised of combinations of the trigonometric functions given in Appendix Appendix A, and that they account for the influence of Poisson's ratio, ν.

Similarly, the process zone of a notch subjected to pure mode n loading can be obtained as above except by using stresses from equation (11) instead of from equation (6). Simplifying and manipulating the resulting expression as before gives

$$\frac{3}{(mS_n)^2} \equiv 3\left(\frac{k}{K_n a^{\lambda_n-1}}\right)^2 = \left(\frac{r_p^n}{a}\right)^{2(\lambda_n-1)} p_n(\theta), \tag{B.2}$$

where $r_p^n(\theta)$ defines the shape of the pure mode n process zone.

To calculate the correlation coefficient between a mixed-mode process zone and pure mode I and pure II zones, ρ_I, ρ_{II}, we first determine the shape of the pure mode I, II process zones, $r_p^I(\theta), r_p^{II}(\theta)$, using equation (B.2). As these are self-similar, we do this simply by fixing $mS_n = 1$. Similarly, to obtain the shape of the mixed-mode process zone, $r_p(\theta)$, we fix G_0/k to a particular value and use equation (B.1). To carry out this calculation, we first discretise these process zones, $r_p(\theta), r_p^I(\theta), r_p^{II}(\theta)$, with respect to θ and then calculate the the correlation coefficients, ρ_I, ρ_{II}, with these discretised process zones. As we are interested in obtaining the values of G_0/k corresponding to particular values of ρ_n, we use a search algorithm that employs a combination of the bisection method and Newton-Raphson iterations for this purpose.

The typical convergence of this technique, i.e. the variation in the value of G_0/k corresponding to any given value of ρ_n with the number of points

used in the discretisation, N, is shown in Figure 13 for the example case of $\rho_{II} = 0.9$ for a 330° notch with $\nu = 0.3$. In the figure, N is varied from 8 to 512 (in multiples of 2), and it is clear that a converged result is obtained for $N = 256$ or greater. Hence, all results are computed at this level of discretisation. We also note that we have explored a range of combinations of α, ν, ρ_n and have found convergence to be insensitive to ν but to be slightly slower for large values of α, ρ. Thus, Figure 13 illustrates close to the slowest convergence within the range of α, ρ considered in our analysis.

Appendix C. Small scale yielding calculation

To calculate the bounds on applied loads that lie within small scale yielding, we approximate the process zone, $r_p(\theta)$, by equating equations (9),(10), substituting in stresses from equations (2),(1), using equation (7), and manipulating and simplifying the resulting expression to give

$$\frac{3}{(mS_I)^2} = \left(\frac{r_p}{a}\right)^{2(\lambda_I-1)} p_I(\theta) + \left(\frac{S_{II}}{S_I}\right)^2 \left(\frac{r_p}{a}\right)^{2(\lambda_{II}-1)} p_{II}(\theta) + \left(\frac{S_{II}}{S_I}\right) \left(\frac{r_p}{a}\right)^{(\lambda_I+\lambda_{II}-2)} p_M(\theta) \tag{C.1a}$$

$$\frac{3}{(mS_{II})^2} = \left(\frac{S_I}{S_{II}}\right)^2 \left(\frac{r_p}{a}\right)^{2(\lambda_I-1)} p_I(\theta) + \left(\frac{r_p}{a}\right)^{2(\lambda_{II}-1)} p_{II}(\theta) + \left(\frac{S_I}{S_{II}}\right) \left(\frac{r_p}{a}\right)^{(\lambda_I+\lambda_{II}-2)} p_M(\theta). \tag{C.1b}$$

We now have two (equivalent) expressions that can be used to calculate the size of the process zone in comparison to the finite dimensions of the geometry under consideration.

To perform this calculation, we choose a particular small scale yielding limit, thus fixing $r_p^{\max}/a$, and we also fix the ratio S_{II}/S_I. We then employ a numerical optimisation that searches equation (C.1a) for the value of θ that minimises mS_I, which occurs when $\theta = \theta^{\max}$, where $\theta^{\max}$ is the angle corresponding to the maximum plastic radius, $r_p^{\max}$, i.e. $r_p^{\max} = r_p(\theta^{\max})$. Thus, we obtain mS_I that corresponds to the specified small scale yielding limit, and, as S_{II}/S_I is known, we can easily calculate the corresponding value of mS_{II}. We must then simply perform this calculation for multiple values of S_{II}/S_I. As this ratio tends to infinity as pure mode I loading conditions are approached, we perform the calculation as described with equation (C.1a) for $0 \leq S_{II}/S_I \leq 1$ and with equation (C.1b) for $0 \leq S_I/S_{II} \leq 1$ to account for the full range of mode-mixities.

Appendix D. Processing of experimental data

To process the experimental data in [22, 14, 23, 16, 24, 17], we require the mode I, II generalised stress intensity factors, K_I, K_{II}, at failure; the characteristic length dimension, a, (see Figure 9); and the shear yield strength of the material, k. Once K_n, a, k are known, we use equation (7) to obtain mS_I, mS_{II}, which we plot in Figure 11. We then use equation (8a) with the values of mS_I, mS_{II} just obtained to calculate G_0/k, which we plot in Figure 12.

In all the papers we considered, the tensile strength, σ_y, of the tested PMMA was reported, but the shear yield strength, k, was not. Thus, we assume the shear yield strength to be given by

$$k = \frac{\sigma_y}{\sqrt{3}} \tag{D.1}$$

in the absence of material data. In Table 1, we record the values of a and σ_y used in our analysis, which we obtained from [14, 23, 16, 24, 17].

We obtained the values of the generalised stress intensity factors at failure in different ways depending on the information reported in each paper. For the data reported by Ayatollahi et al. [17], we used image extrapolation software to infer the generalised stress intensities at failure directly from Figure 8 in [17]. Both mode I, II generalised stress intensities in this figure are normalised by the *critical mode I generalised stress intensity factor* denoted K_{Ic}^V in [17] (which is distinct from the *fracture toughness* denoted K_{Ic} in [17]). To obtain the actual values of the generalised stress intensity at failure, we calculated K_{Ic}^V from equations (8),(11) in [17] using the values of fracture toughness ($K_{Ic} = 1.96MPa\sqrt{m}$) and tensile strength (see Table 1) reported in [17]. From equations (4),(A1),(A2) in [17], it can be seen that the authors use the same normalisation of the angular eigenfunctions as in our formulation, so no rescaling is required.

For the data reported by Dunn et al. [23], we used image extrapolation software to obtain calibrations for the generalised stress intensity factors from Figure 5 in [23]. We then used equation (5) in [23] with the failure loads reported in Table 3 in [23]. Unfortunately, we were unable to find explicit mention of what scaling was applied to the angular eigenfunctions. However, we assume that Dunn et al. [23] used the typical normalisation of $f_{\theta\theta}^I(0) = 1$ and $f_{r\theta}^{II}(0) = 1$ because this normalisation is used in several other papers by the authors around the same period [15, 26, 27]. As this is the same scaling used in our formulation, no rescaling is required.

For the tests conducted by Kim and Cho [24], we used image extrapolation software to infer the mode I, II generalised stress intensities at failure

(denoted K^n_{Icr}, K^n_{IIcr} in [24]) directly from Figure 10 in [24]. However, the formulation used by Kim and Cho [24] does not normalise the angular eigenfunctions in the same way as in our formulation and also pulls out a factor of $1/\sqrt{2\pi}$ as shown in equation (4) in [24]. Thus, we must rescale the generalised stress intensity factors inferred from Figure 10 in [24] (i.e. K^n_{Icr}, K^n_{IIcr} in [24]) to match those used in our formulation. To do this, we multiply the obtained values of K^n_{Icr} and K^n_{IIcr} by $f^I_{\theta\theta n}(\theta = 0)/\sqrt{2\pi}$ and $f^{II}_{r\theta n}(\theta = 0)/\sqrt{2\pi}$, respectively, where $f^I_{\theta\theta n}(\theta = 0)$ and $f^I_{r\theta n}(\theta = 0)$ are the angular eigenfunctions used in [24] evaluated along the notch bisector. These angular eigenfunctions are written out explicitly below equation (2) in [24].

For the tests reported by Priel et al. [16], the ratio of the generalised stress intensities, K_{II}/K_I, (denoted A_2/A_1 in [16]) is given in Table 5 in [16]. The value of the mode I generalised stress intensity at failure is given in Table 10 in [16] (and is denoted A_1 in [16]). This information enables the value of the mode II generalised stress intensity at failure to be calculated easily. From equation (5) in [16], it is clear that Priel et al. [16] normalise the angular eigenfunctions in the same way as in our formulation, so no rescaling is required.

For the data reported by Seweryn et al. [22], slightly different calibrations of the generalised stress intensity factors are reported in [22, 14]. The latter set of calibrations were obtained using a more refined model and are more accurate. Hence, we have use this latter set of calibrations, which are given in Table 1 of [14], along with the failure loads reported in Table 2 in [22] to determine the generalised stress intensity factors at failure. From [22, 14, 28], it is clear that the authors use the same normalisation of the angular eigenfunctions as is used as in our formulation. However, from equation (1) in [14] we see that their formulation differs from ours by a factor of $(2\pi)^{\lambda-1}$. Thus, we must multiply the obtained generalised stress intensity factors by $(2\pi)^{\lambda-1}$ to rescale them for our formulation.

Captions to figures

1. An idealised diagram of a semi-infinite notch of interior angle 2α showing the polar coordinate set (r, θ) and both lobes of the plastic zone, $r_{p1}(\theta), r_{p2}(\theta)$.
2. A plot of the order of the mode I, II singularities against notch angle, 2α.
3. A Cartesian plot of r vs. θ displaying the relative *shape* of: (a) a pure mode I process zone, r^I_p, and a mixed-mode process zone, r_p, of $G_0/k = 0.2495$, and (b) a pure mode II process zone, r^{II}_p, and a mixed-mode process zone, r_p, of $G_0/k = 1.292$. These process zones

are computed for the example of a 270° notch with $\nu = 0.3$ and result in $\rho_I, \rho_{II} = 0.7$ in plot (a),(b), respectively.

4. A plot of showing the correlation coefficients, ρ_I, ρ_{II}, (when positive), vs. G_0/k for a notch of $2\alpha = 270°$ and $\nu = 0.3$, which illustrates the variation of the mode-mixity of the process zone with the applied load. The range of applied loads for which the process zone is mode I dominated, mode II dominated, or mixed-mode are shown (assuming $\rho_I, \rho_{II} = 0.7$ mark these boundaries).
5. Plots of G_0/k against notch angle, 2α, showing the mode-mixity of the process zone for four choices of ρ_I, ρ_{II}, viz. $0.95, 0.9, 0.8, 0.7$, when $\nu = 0.3$.
6. Plots in dimensionless generalised stress intensity space, i.e. mS_{II} vs. mS_I, showing the mode-mixity of the process zone (a) for four choices of ρ_I, ρ_{II}, viz. $0.95, 0.9, 0.8, 0.7$, when $2\alpha = 270°$ and $\nu = 0.3$ and (b) for three different notch angles, viz. $2\alpha = 270°, 300°, 330°$, when $\nu = 0.3$ and $\rho_I, \rho_{II} = 0.9$.
7. A plot of mS_{II} vs. mS_I that shows the values of generalised stress intensity factors that result in $r_{p1}^{\max}, r_{p2}^{\max} = 0.1a$ for the example case of $2\alpha = 270°$ and $\nu = 0.3$. The shaded area shows the region in which both plastic lobes, $r_{p1}^{\max}, r_{p2}^{\max}$, are within small scale yielding.
8. Plots of mS_{II} vs. mS_I showing small scale yielding limits (a) for four choices of $r_p^{\max}/a$, viz. $0.01, 0.05, 0.1, 0.15$, when $2\alpha = 270°$ and $\nu = 0.3$ and (b) for three different notch angles, viz. $2\alpha = 270°, 300°, 330°$, when $\nu = 0.3$ and $r_p^{\max}/a = 0.1$.
9. Diagrams (not to scale) of the selected test geometries. The applied loads and the dimension we have selected as the characteristic length, a, are also shown.
10. Plots showing the influence of Poisson's ratio (a) on the mode-mixity results for $\rho_I, \rho_{II} = 0.9$ and (b) on the small scale yielding results for $r_p^{\max}/a = 0.1$, both for the example case of a 270° notch.
11. Plots of mS_{II} vs. mS_I that show the state of generalised stress intensity at failure for the fracture test data reported in [22, 23, 16, 24, 17]. Mode-mixity results for $\rho_I, \rho_{II} = 0.95, 0.9, 0.8, 0.7$ and small scale yielding results for $r_p^{\max}/a = 0.01, 0.05, 0.1, 0.15$ are also shown (all calculated assuming $\nu = 0.36$).
12. A plot of all the mixed-mode data from Figure 11, which shows the mode-mixity of the process zone for $\rho_I, \rho_{II} = 0.95, 0.9, 0.8, 0.7$ (calculated assuming $\nu = 0.36$).
13. A plot of the typical convergence of ρ with the number of points used in the discretisation, N, for the example case of $\rho_{II} = 0.9$, $\nu = 0.3$, and $2\alpha = 330°$.

Captions to tables

1. The values of the characteristic length, a, and tensile strength, σ_y, used in our analysis.

Tables

Author	Test group	a (mm)	σ_y (MPa)
Ayatollahi et al. [17]	270°	14.142	70.5
	300°	11.547	70.5
	330°	10.353	70.5
Dunn et al. [23]	270°	2.54	69.8
	270°	5.08	69.8
	270°	7.62	69.8
	270°	10.16	69.8
Kim and Cho [24]	270°	20	61.7
	285°	20	61.7
	300°	20	61.7
	330°	20	61.7
Priel et al. [16]	315° at $198K$	3.266	179.5
	315° at $296K$	3.788	111.8
Seweryn and Łukaszewicz [14]	280°	25	102.8
	300°	25	102.8
	320°	25	102.8

Table D.1: The values of the characteristic length, a, and tensile strength, σ_y, used in our analysis.

Figure1

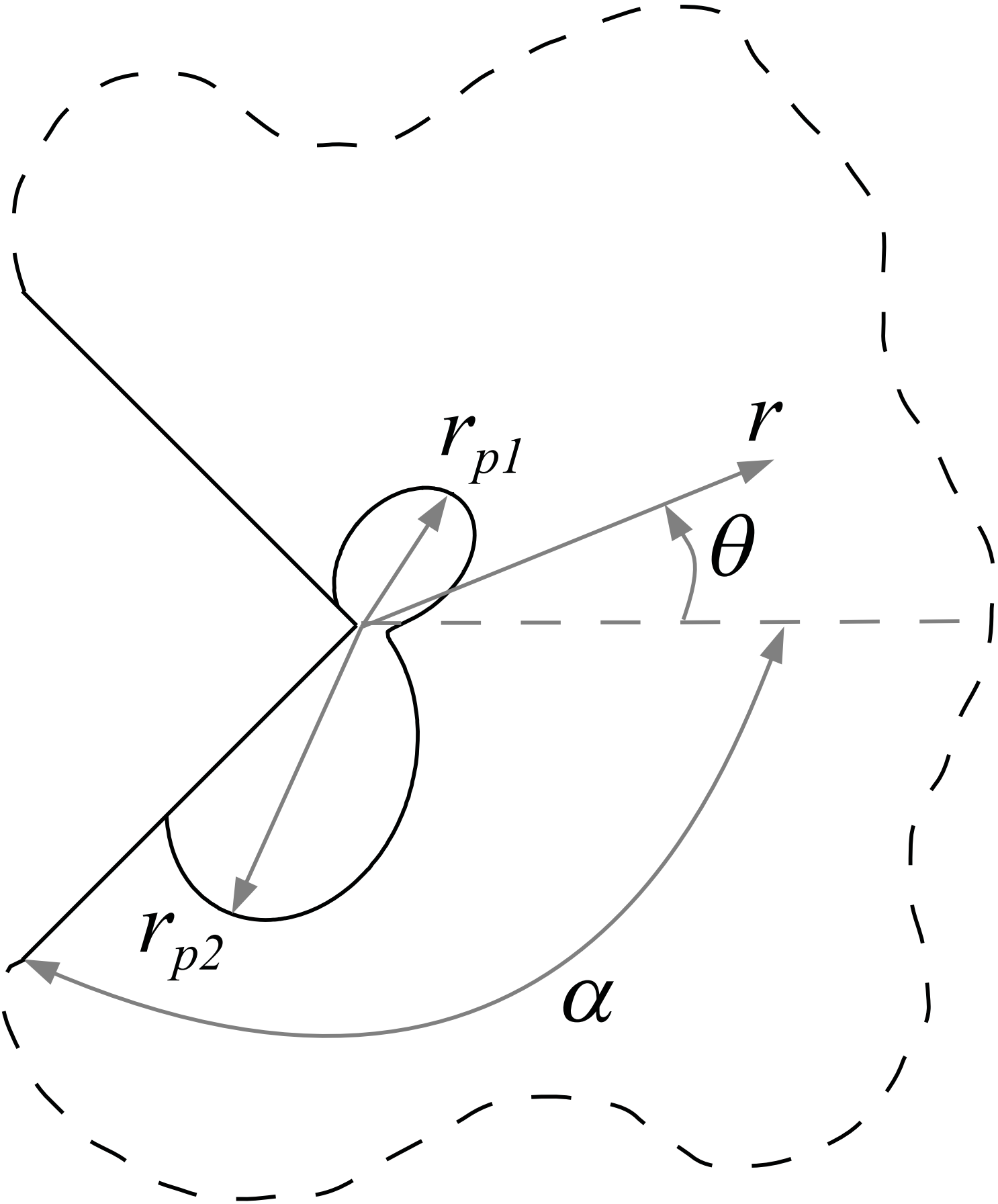

Figure2

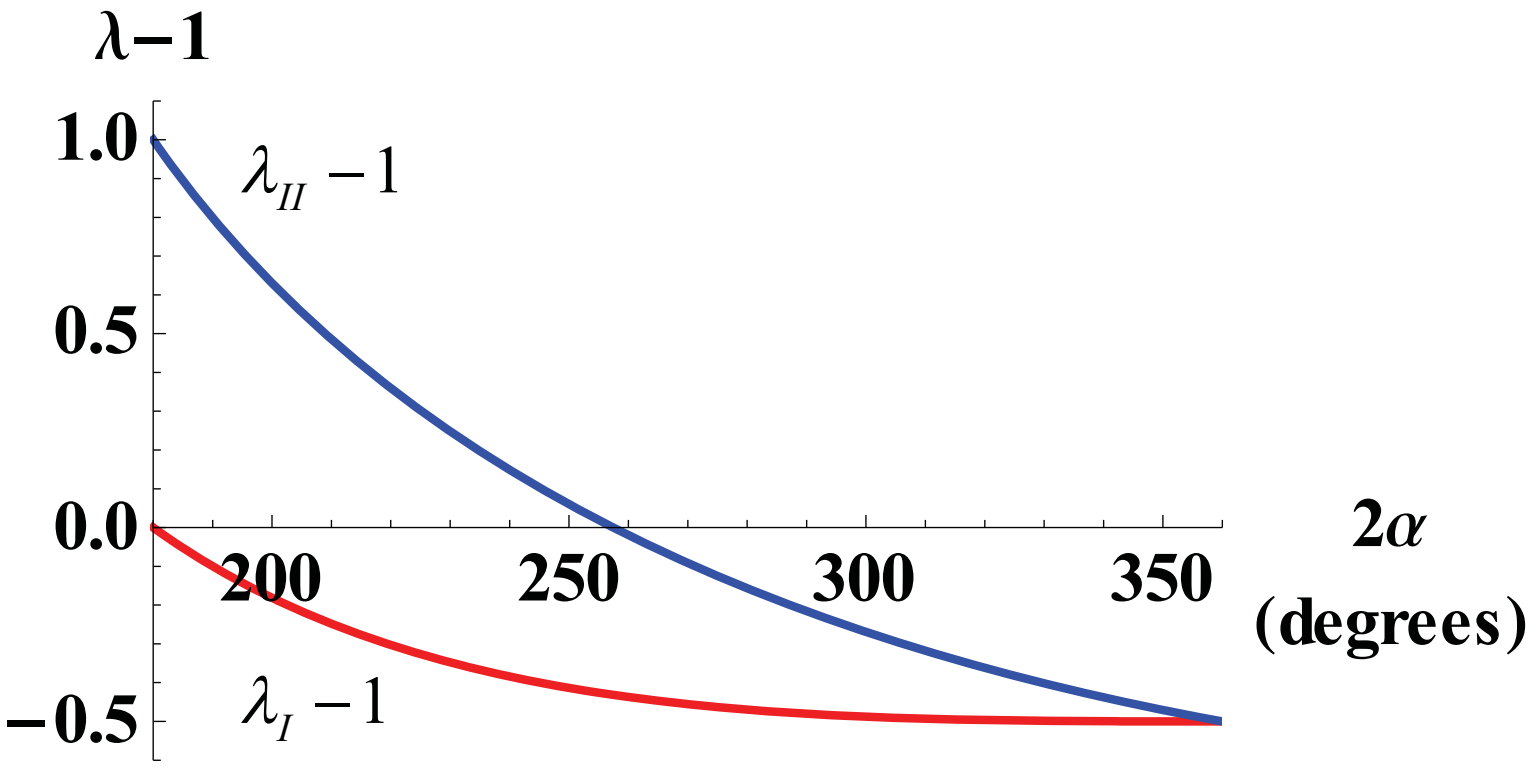

Figure3a

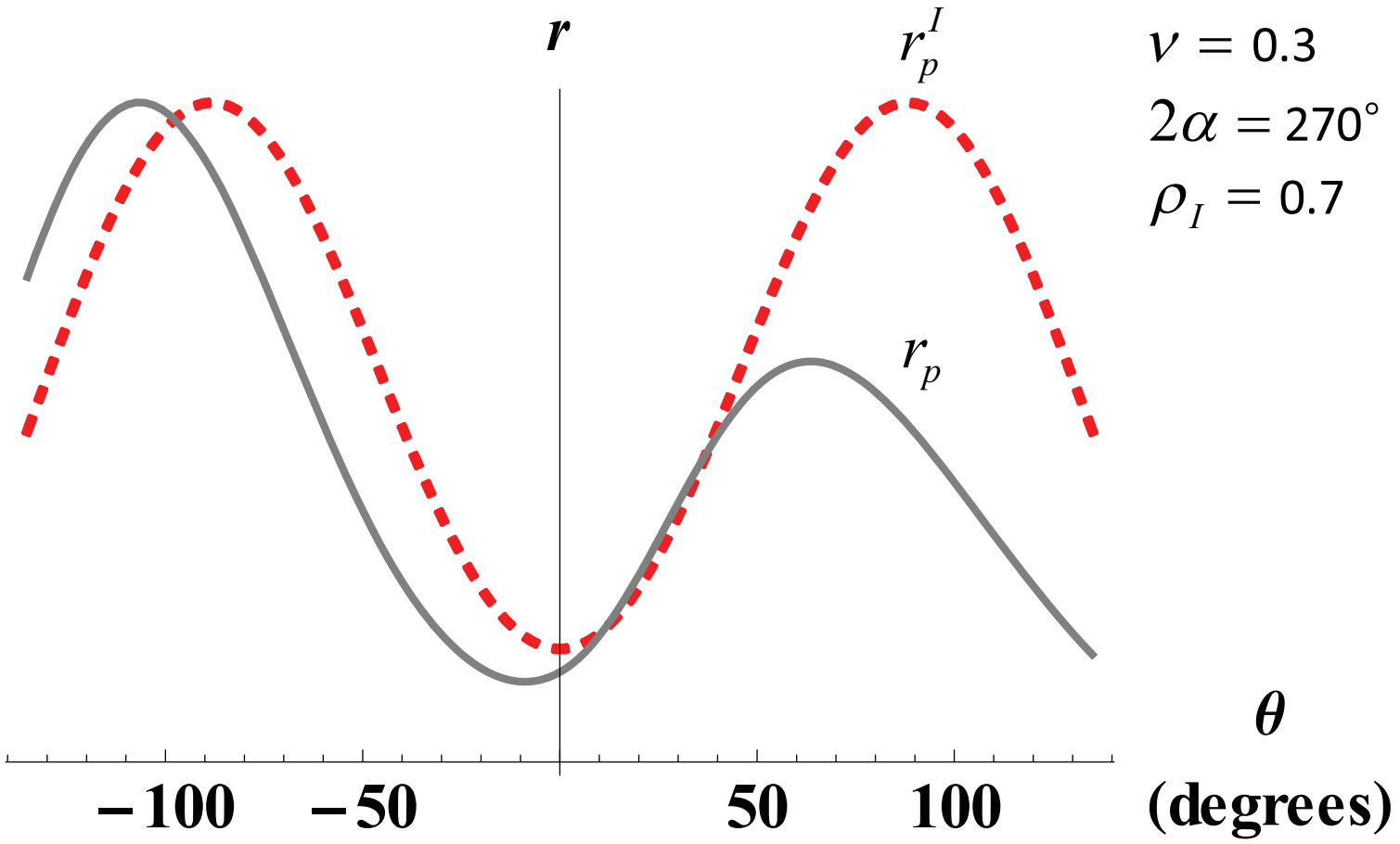

Figure3b

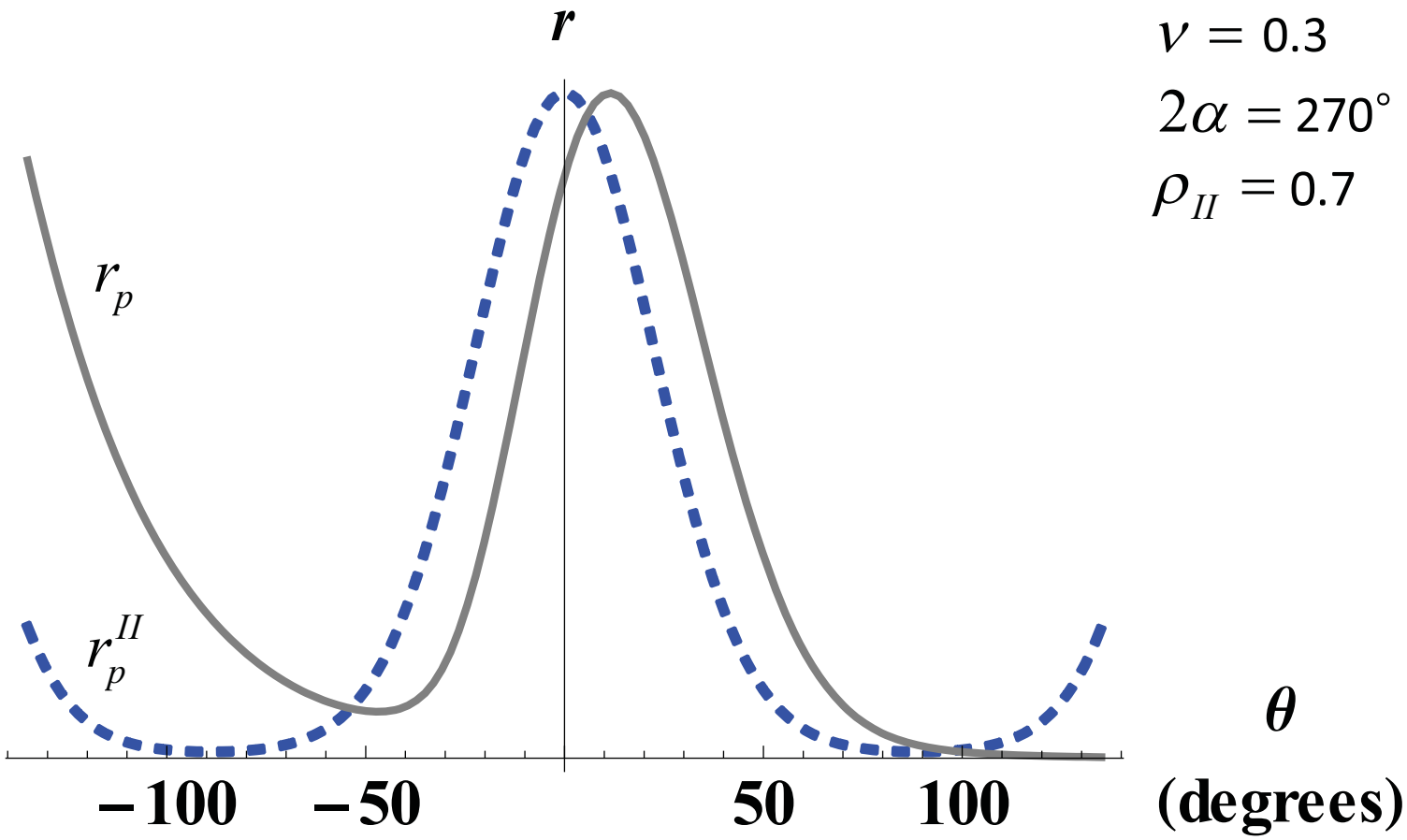

Figure4

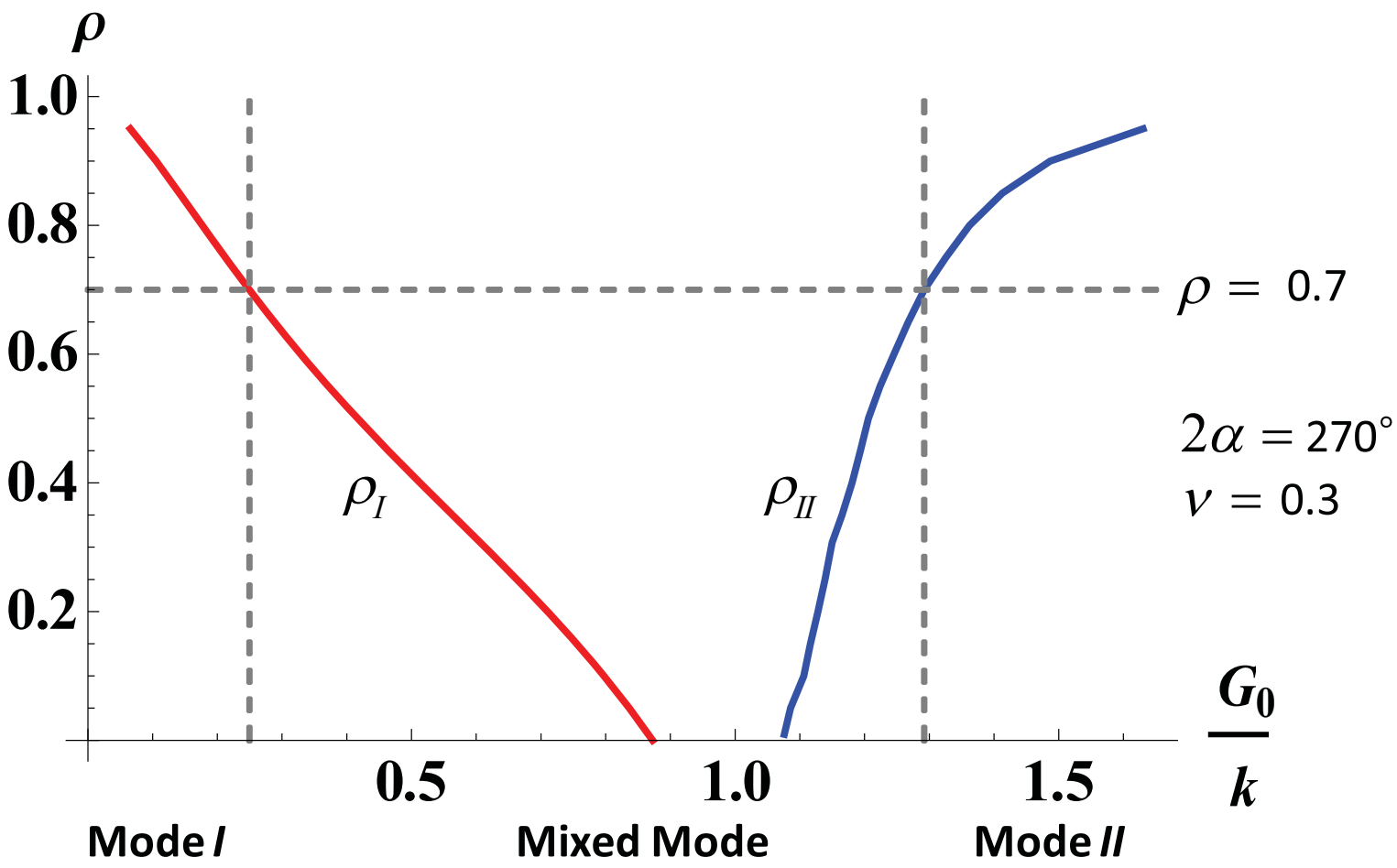
ρ
1.0
0.8
0.6
0.4
0.2
ρ = 0.7
2α = 270°
ν = 0.3
ρ_I
ρ_II
G_0 / k
0.5
1.0
1.5
Mode I
Mixed Mode
Mode II

Figure5

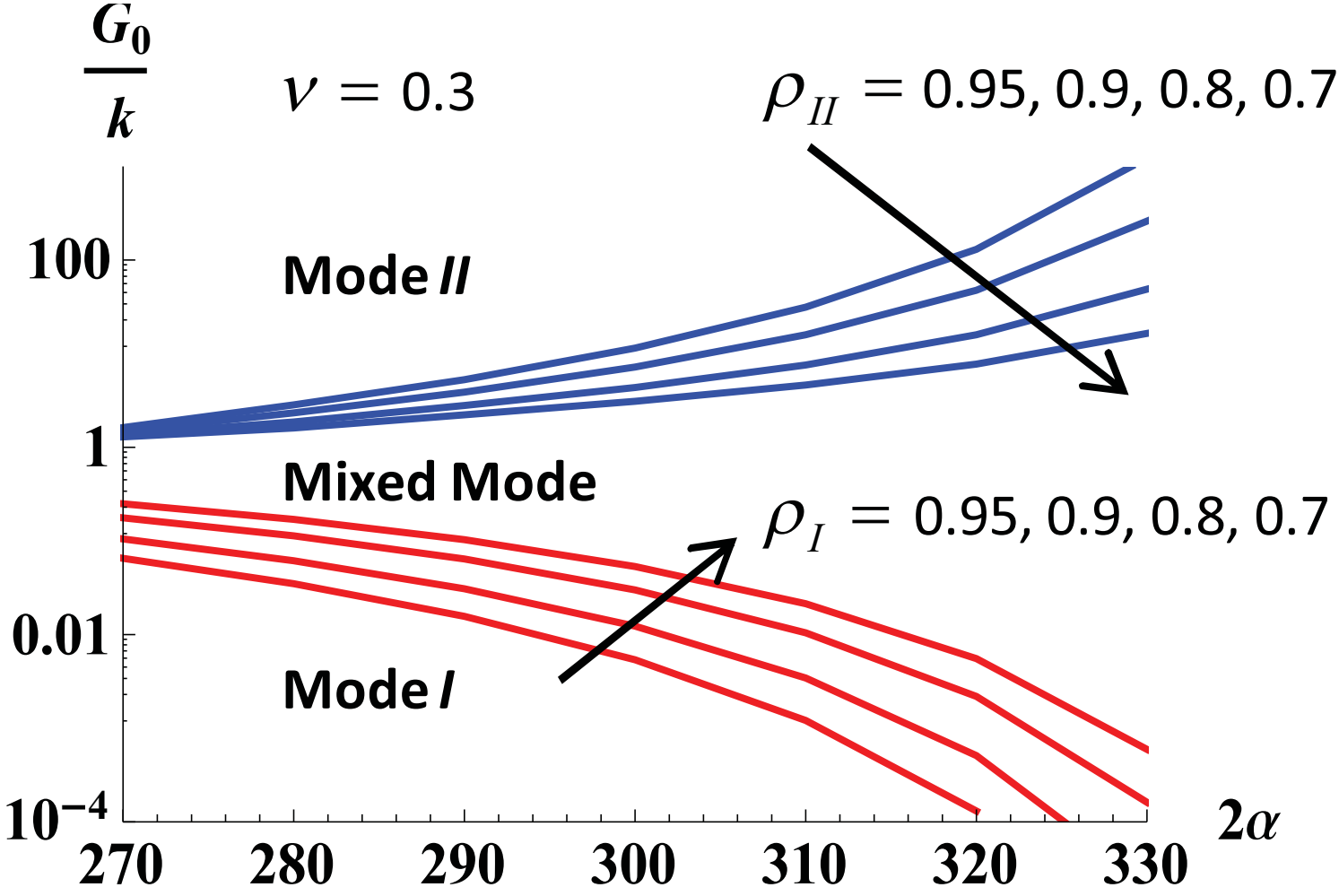
$\frac{G_0}{k}$
$\nu = 0.3$
$\rho_{II} = 0.95, 0.9, 0.8, 0.7$
100
Mode II
1
Mixed Mode
$\rho_I = 0.95, 0.9, 0.8, 0.7$
0.01
Mode I
10^{-4}
270
280
290
300
310
320
330
2α

Figure6a

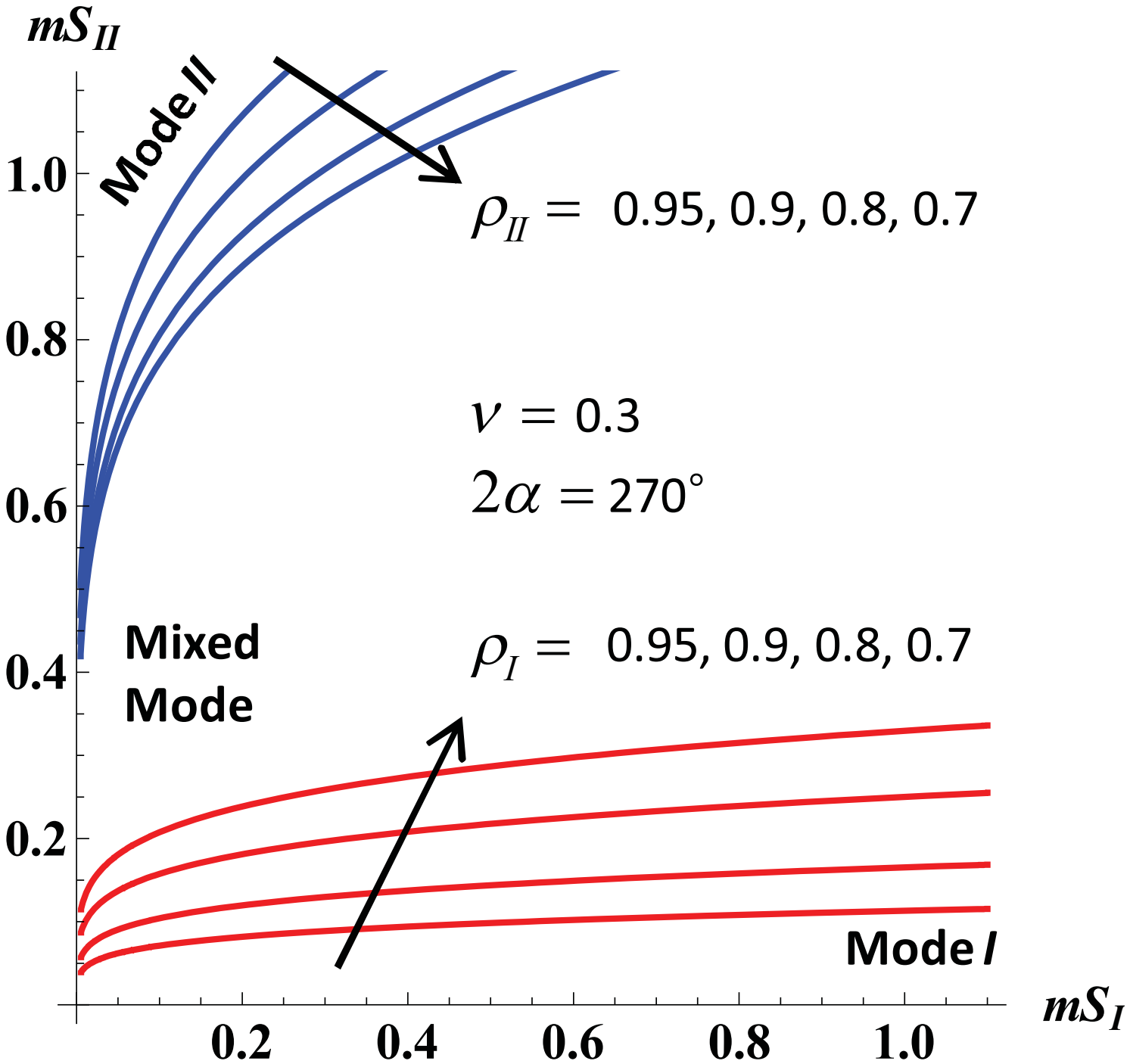
mS_{II}
Mode II
1.0
0.8
0.6
0.4
0.2
$\rho_{II} =$ 0.95, 0.9, 0.8, 0.7
$\nu = 0.3$
$2\alpha = 270°$
Mixed Mode
$\rho_I =$ 0.95, 0.9, 0.8, 0.7
Mode I
0.2
0.4
0.6
0.8
1.0
mS_I

Figure6b

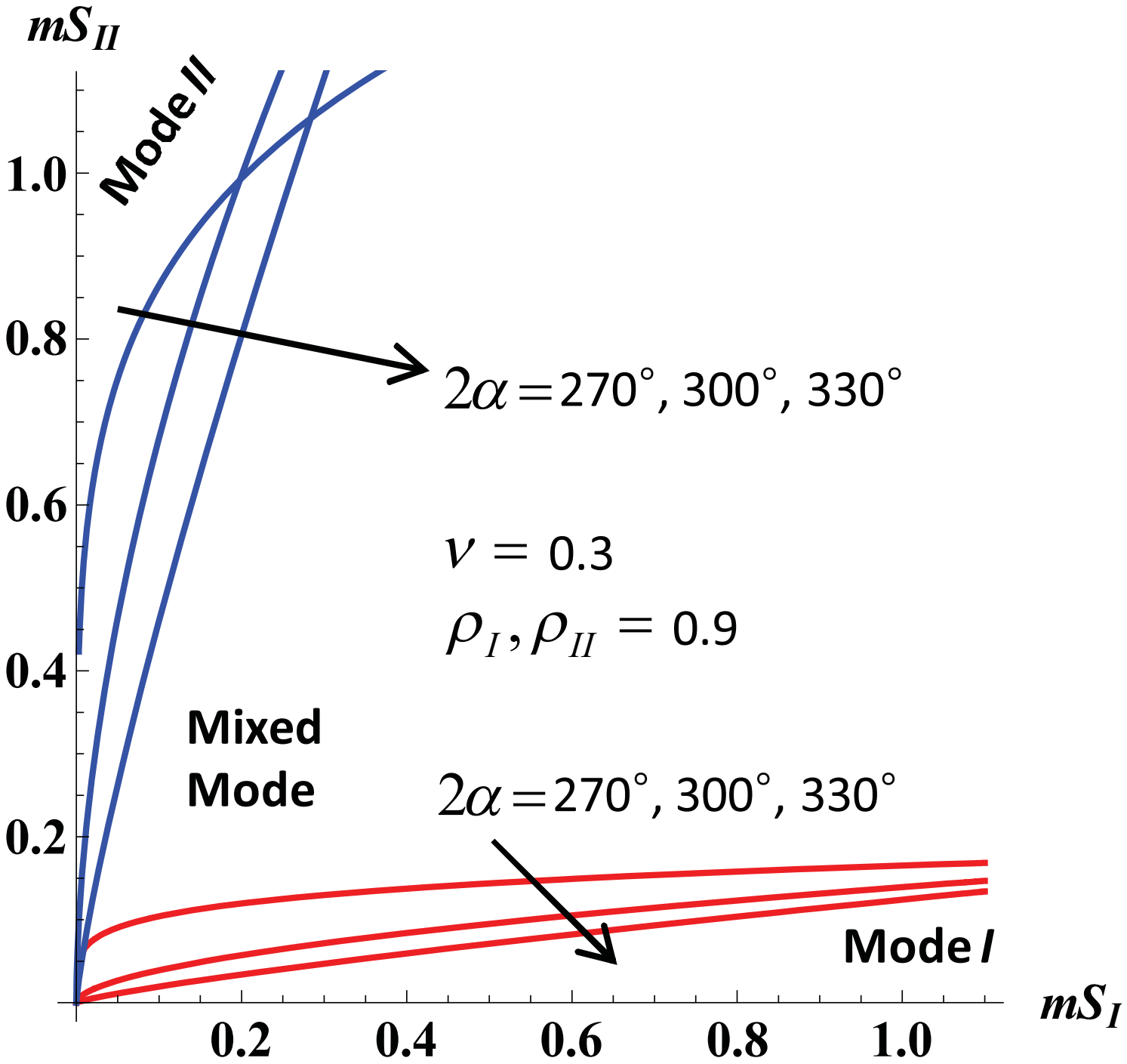
mS_{II}
Mode II
1.0
0.8
0.6
0.4
0.2
$2\alpha = 270^\circ, 300^\circ, 330^\circ$
$\nu = 0.3$
$\rho_I, \rho_{II} = 0.9$
Mixed Mode
$2\alpha = 270^\circ, 300^\circ, 330^\circ$
Mode I
mS_I
0.2
0.4
0.6
0.8
1.0

Figure7

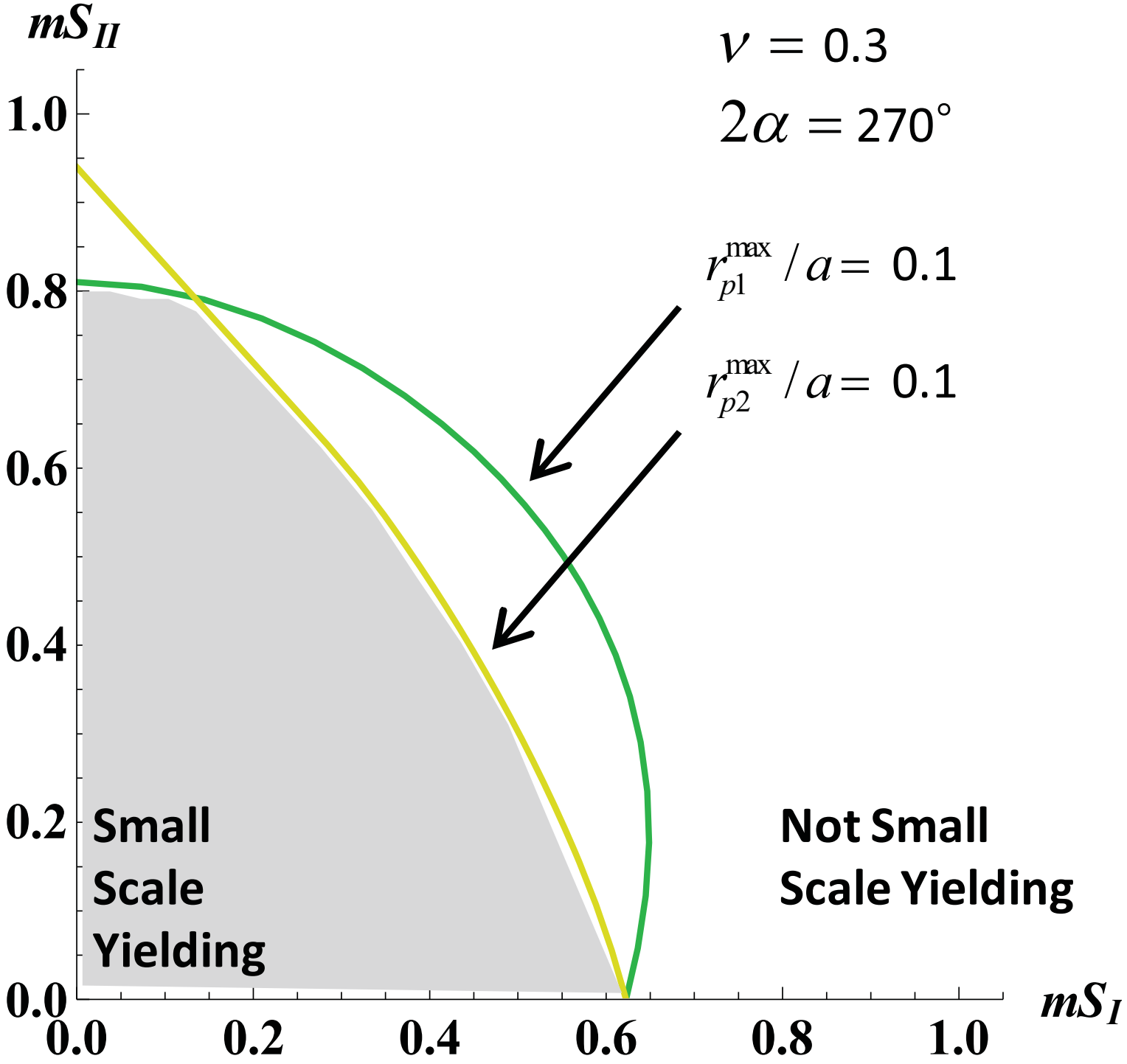
mS_{II}
$\nu = 0.3$
$2\alpha = 270°$
$r_{p1}^{\max} / a = 0.1$
$r_{p2}^{\max} / a = 0.1$
1.0
0.8
0.6
0.4
0.2
0.0
Small Scale Yielding
Not Small Scale Yielding
0.0
0.2
0.4
0.6
0.8
1.0
mS_I

Figure8a

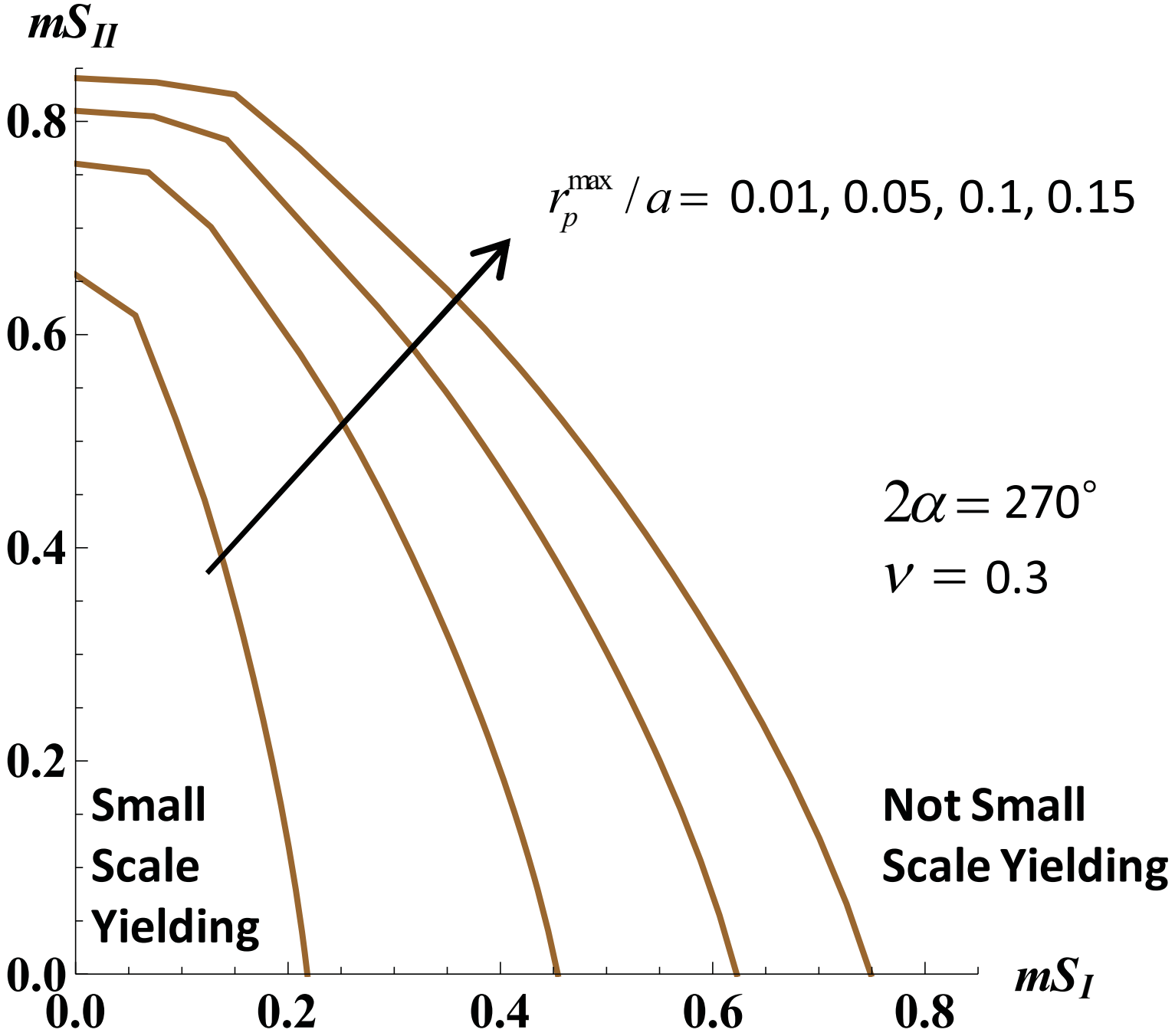
mS_{II}
0.8
0.6
0.4
0.2
0.0
$r_p^{\max}/a =$ 0.01, 0.05, 0.1, 0.15
$2\alpha = 270^\circ$
$\nu = 0.3$
Small Scale Yielding
Not Small Scale Yielding
mS_I
0.0
0.2
0.4
0.6
0.8

Figure8b

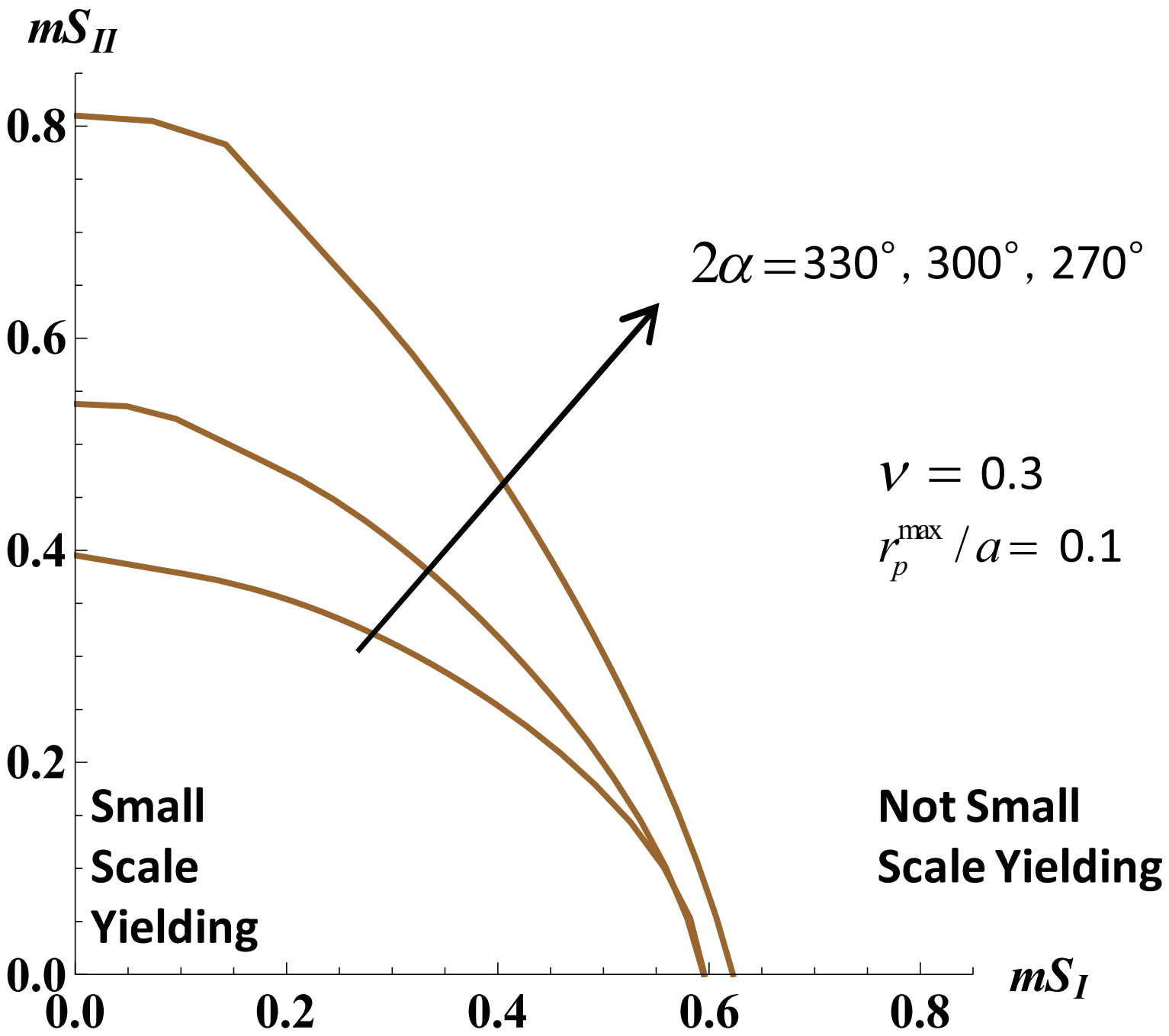
mS_{II}
0.8
0.6
0.4
0.2
0.0
0.0
0.2
0.4
0.6
0.8
mS_I
$2\alpha = 330^\circ, 300^\circ, 270^\circ$
$\nu = 0.3$
$r_p^{\max} / a = 0.1$
Small Scale Yielding
Not Small Scale Yielding

Figure9

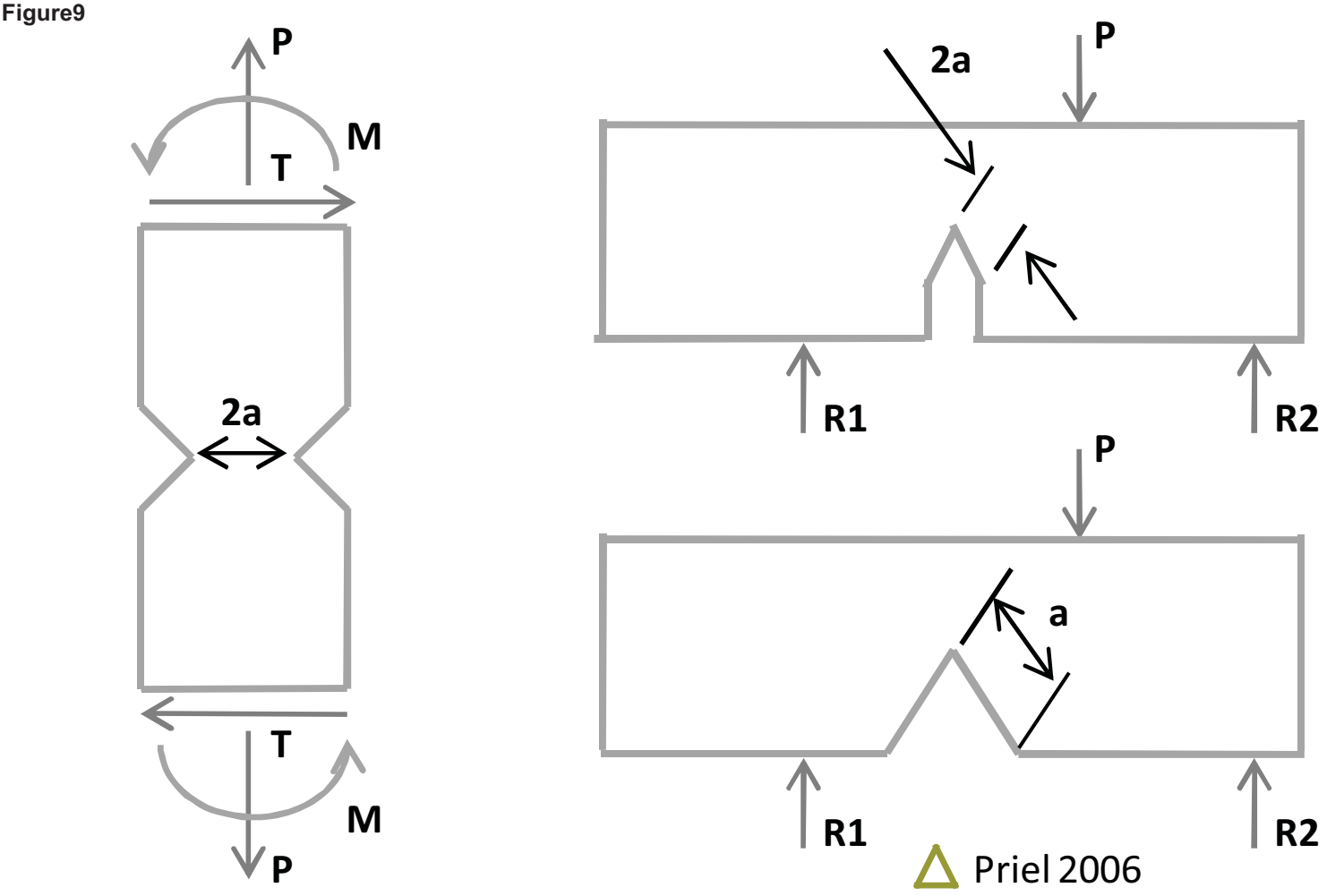
P
M
T
2a
T
M
P
2a
P
R1
R2
P
a
R1
R2
Priel 2006
Seweryn 2002

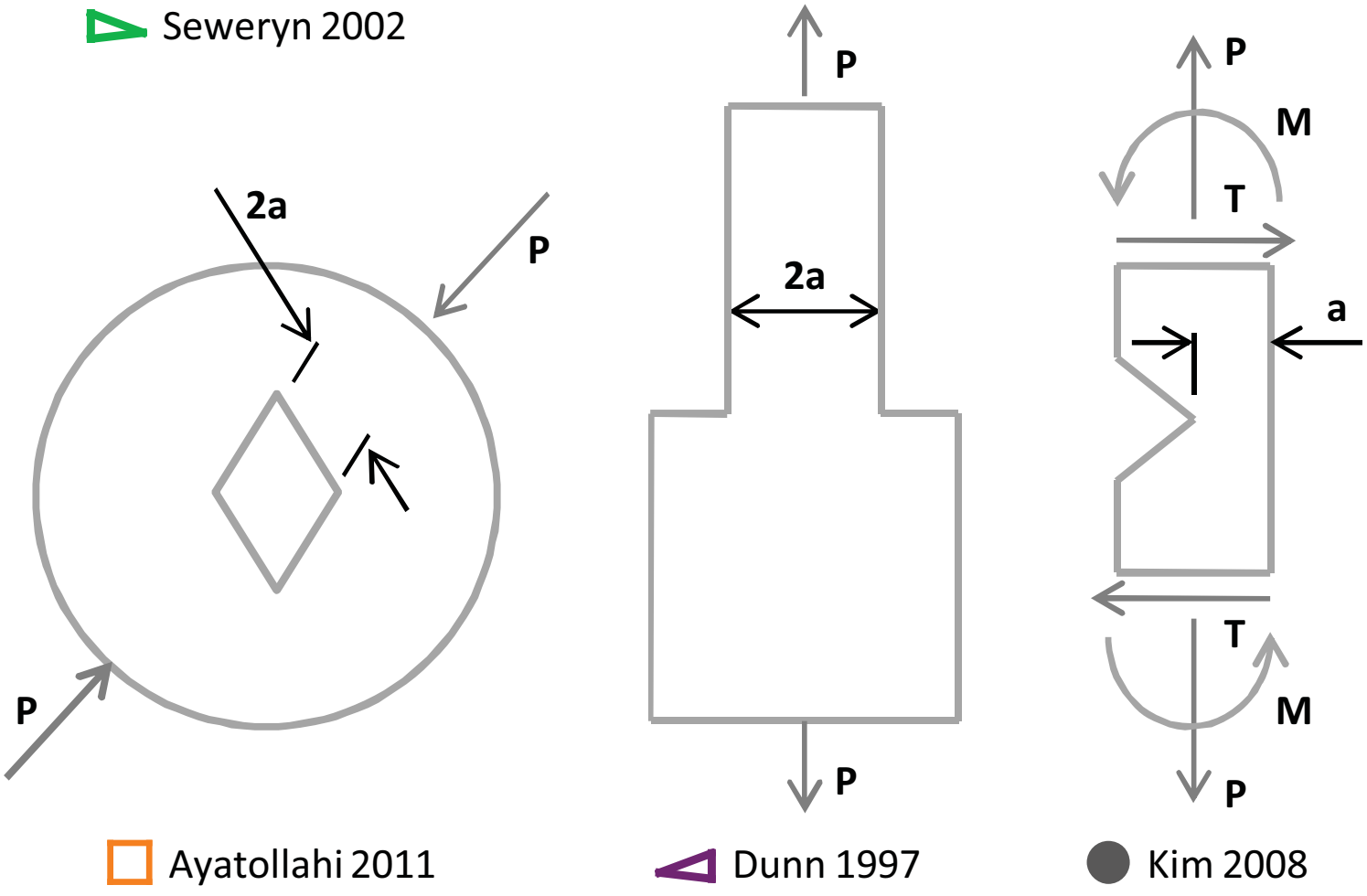
2a
P
P
P
2a
P
P
M
T
a
T
M
P
Ayatollahi 2011
Dunn 1997
Kim 2008

Figure10a

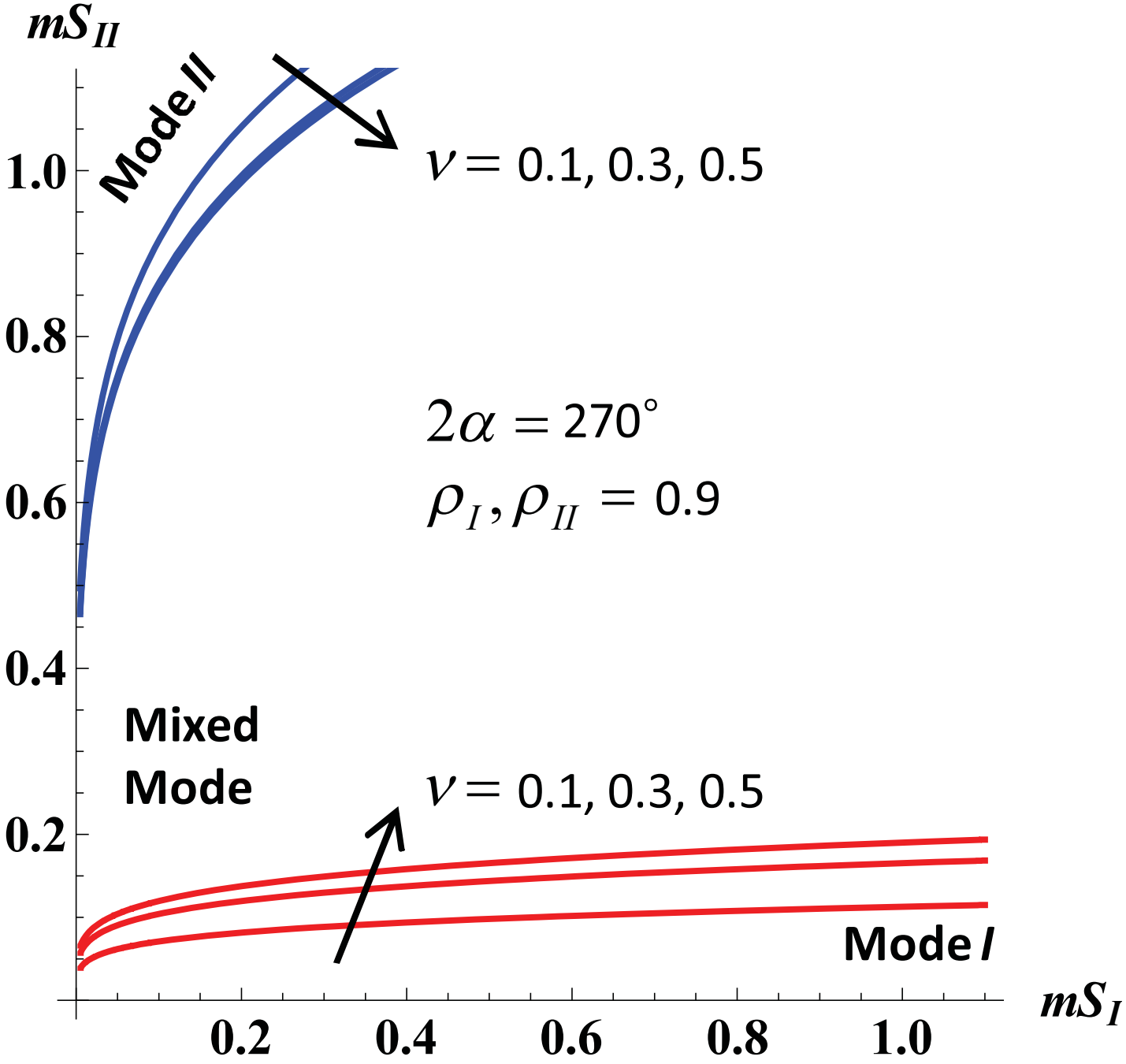
mS_{II}
Mode II
1.0
0.8
0.6
0.4
0.2
$\nu = 0.1, 0.3, 0.5$
$2\alpha = 270^\circ$
$\rho_I, \rho_{II} = 0.9$
Mixed
Mode
$\nu = 0.1, 0.3, 0.5$
Mode I
mS_I
0.2
0.4
0.6
0.8
1.0

Figure10b

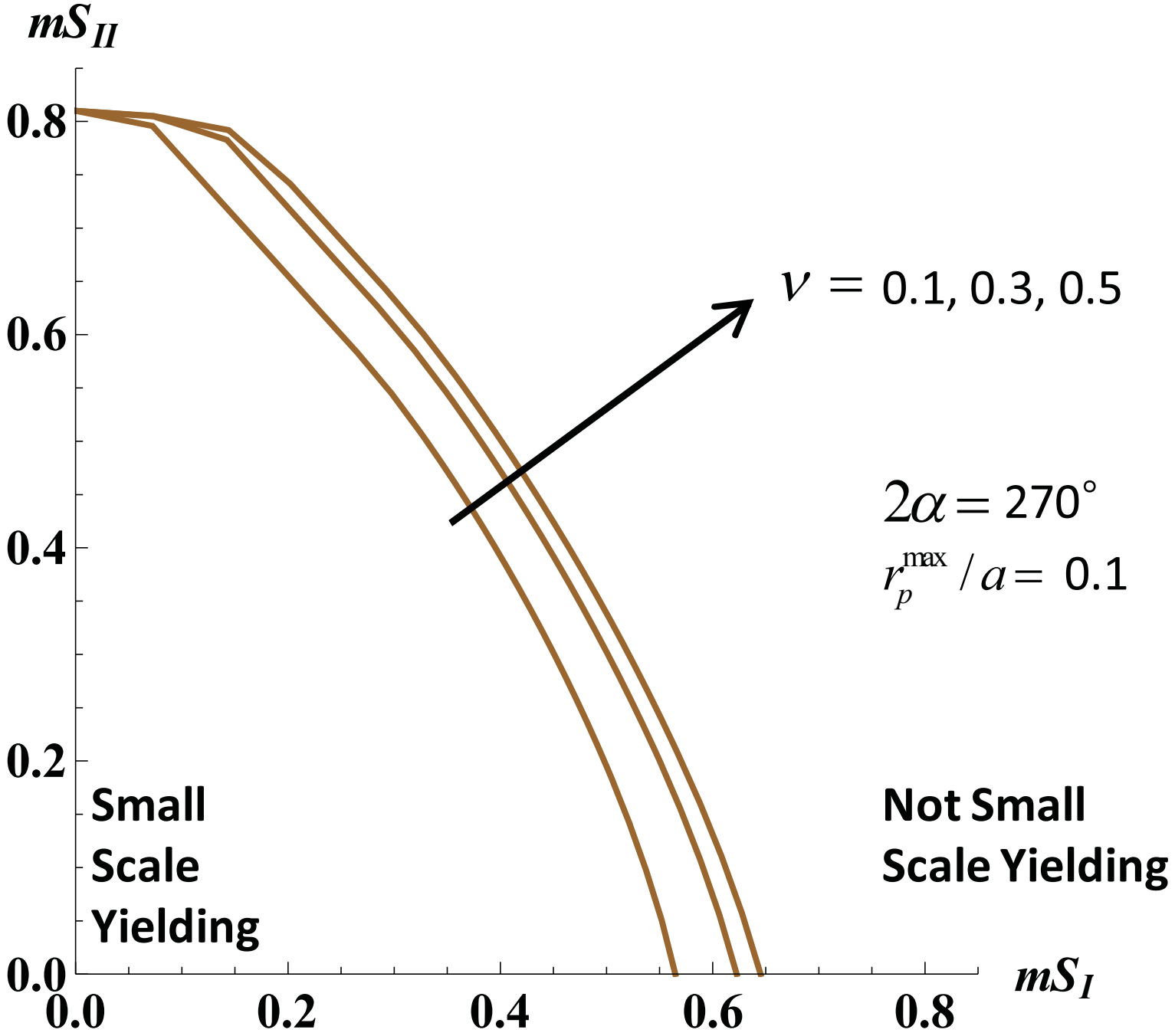
mS_{II}
0.8
0.6
0.4
0.2
0.0
0.0
0.2
0.4
0.6
0.8
mS_I
$\nu = 0.1, 0.3, 0.5$
$2\alpha = 270^\circ$
$r_p^{\max} / a = 0.1$
Small Scale Yielding
Not Small Scale Yielding

Figure11a

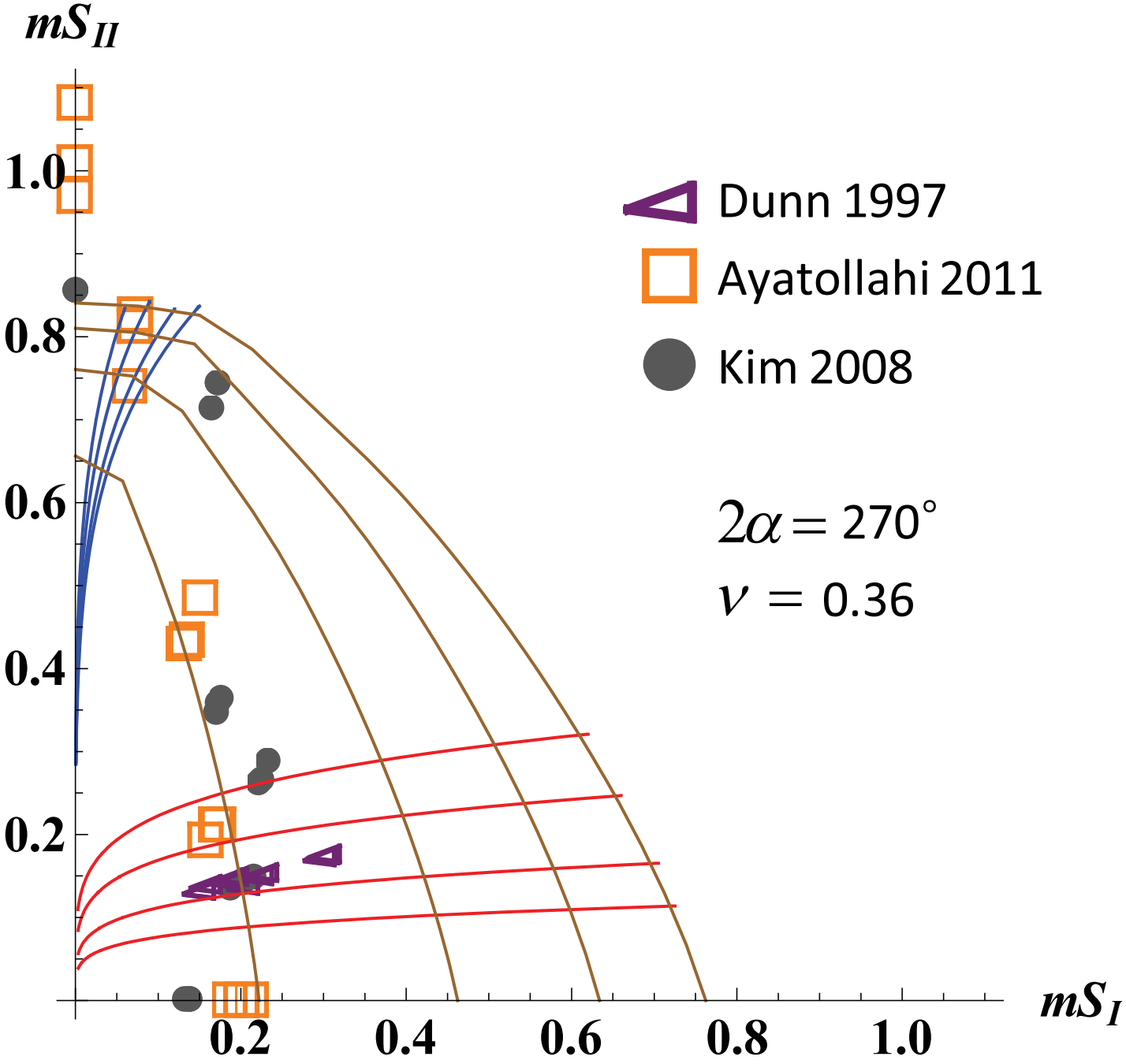
mS_{II}
1.0
0.8
0.6
0.4
0.2
0.2
0.4
0.6
0.8
1.0
mS_I
Dunn 1997
Ayatollahi 2011
Kim 2008
$2\alpha = 270^\circ$
$\nu = 0.36$

Figure11b

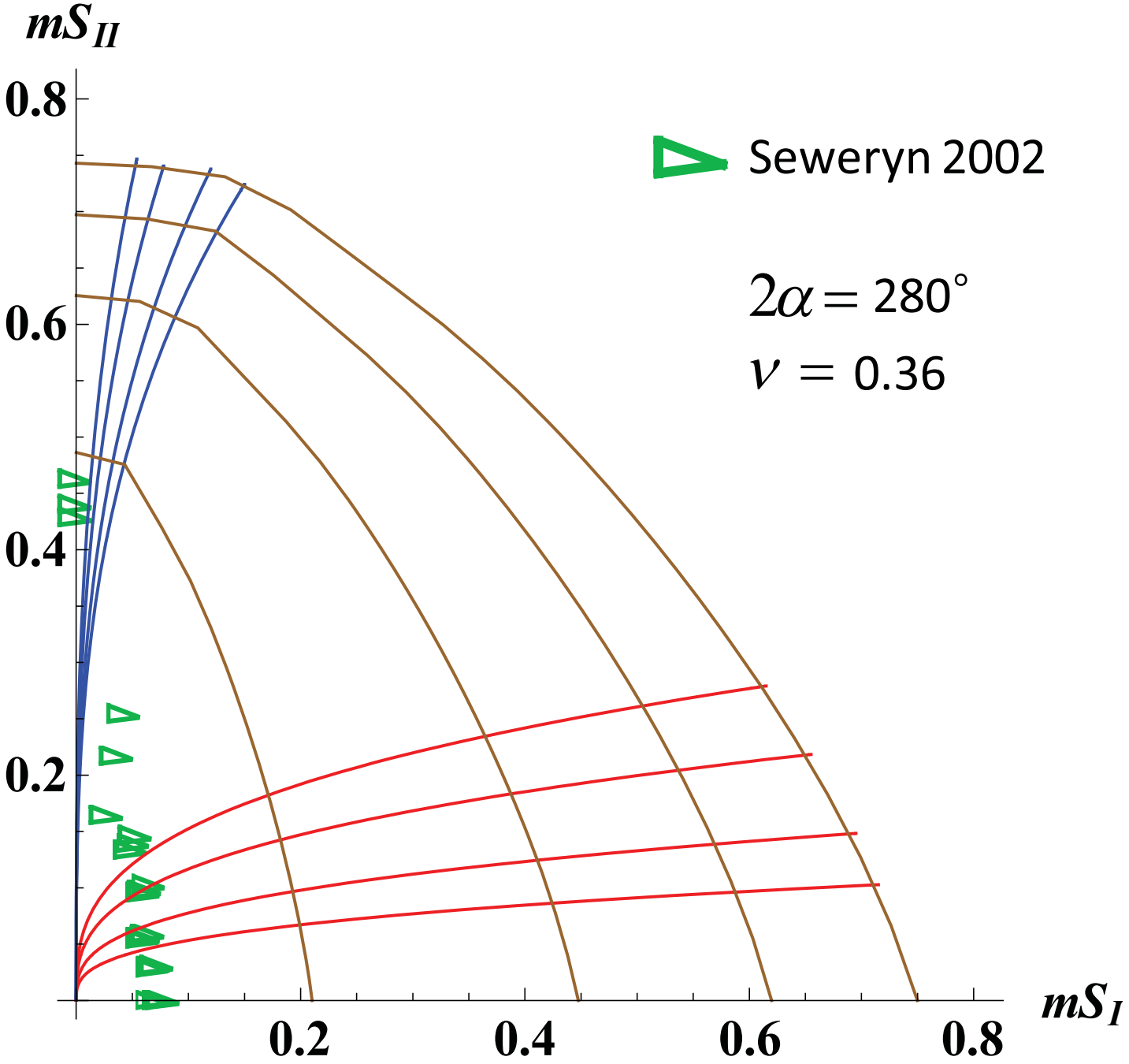
mS_{II}
0.8
0.6
0.4
0.2
0.2
0.4
0.6
0.8
mS_I
Seweryn 2002
$2\alpha = 280^\circ$
$\nu = 0.36$

Figure11c

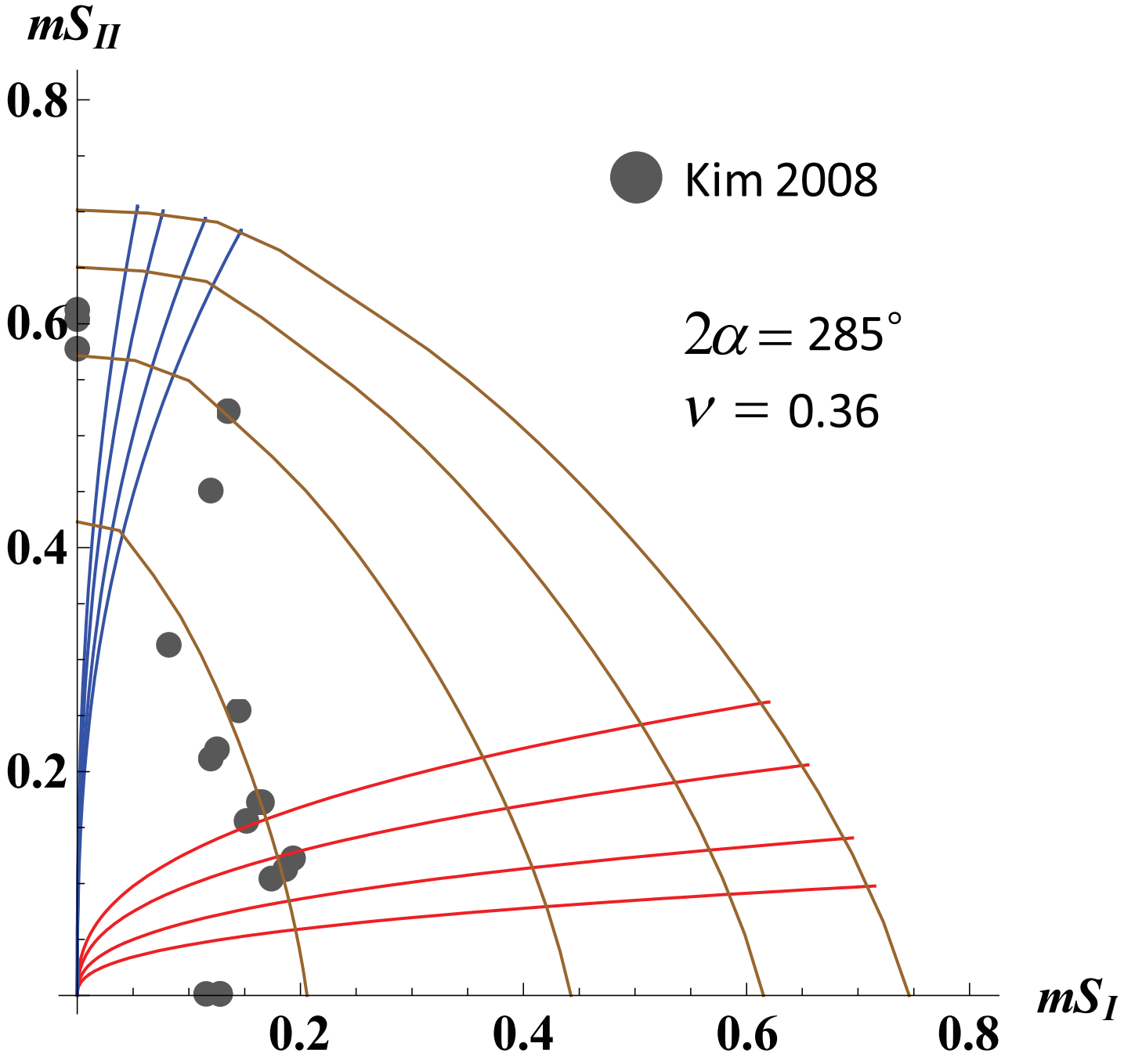

Figure11d

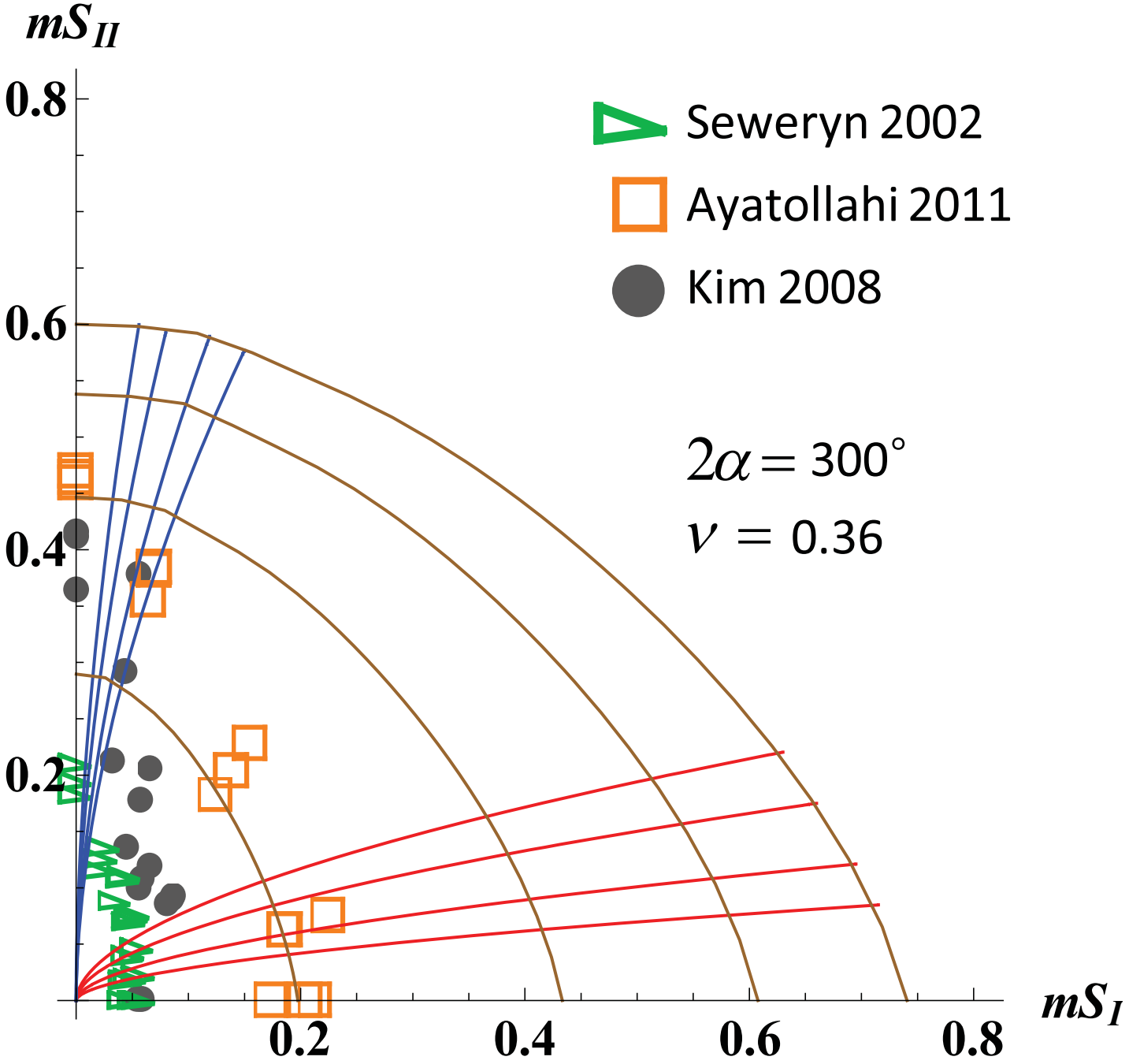
mS_{II}
0.8
0.6
0.4
0.2
0.2
0.4
0.6
0.8
mS_I
Seweryn 2002
Ayatollahi 2011
Kim 2008
$2\alpha = 300^\circ$
$\nu = 0.36$

Figure11e

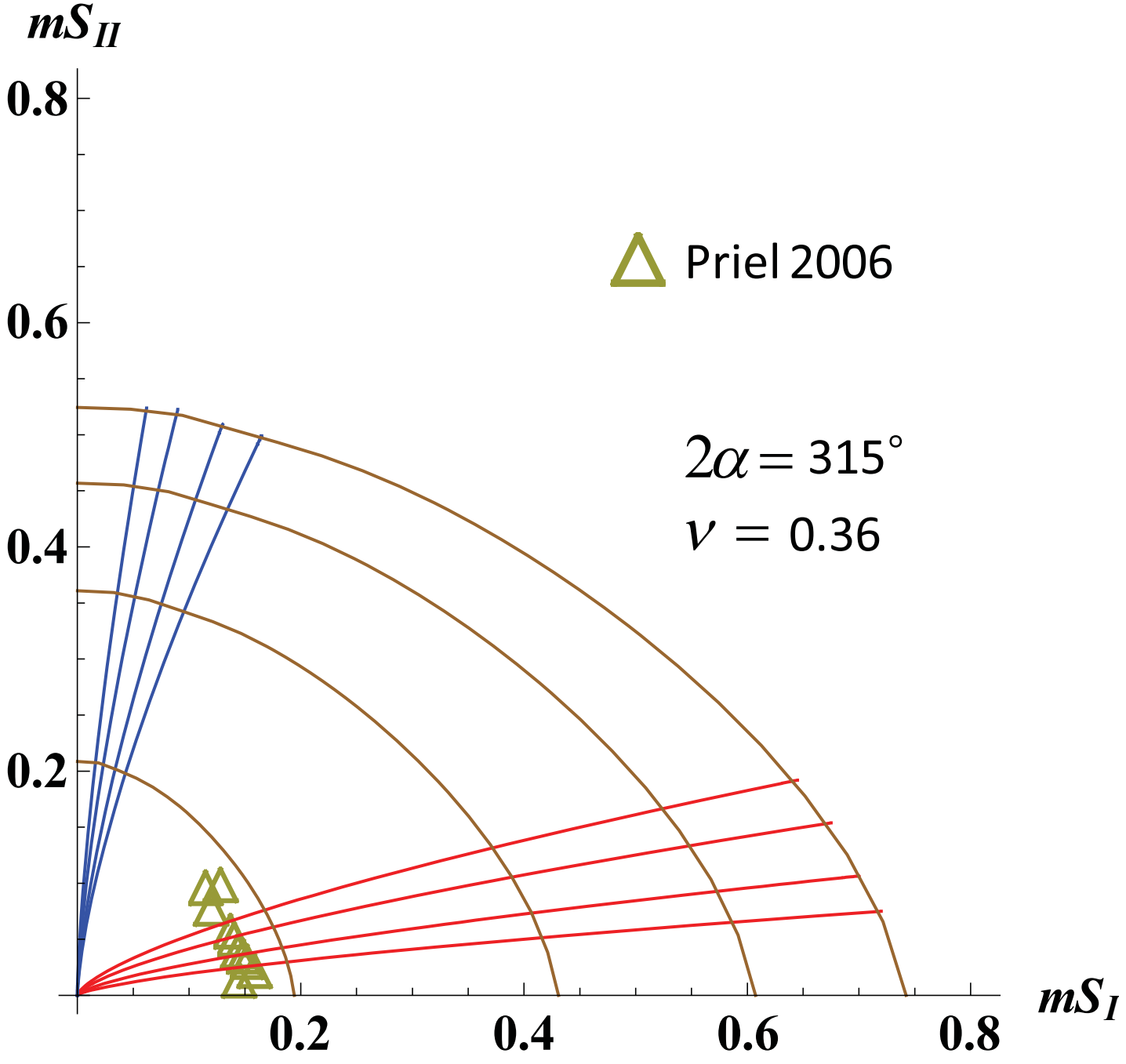
mS_{II}
0.8
0.6
0.4
0.2
Priel 2006
$2\alpha = 315^\circ$
$\nu = 0.36$
0.2
0.4
0.6
0.8
mS_I

Figure11f

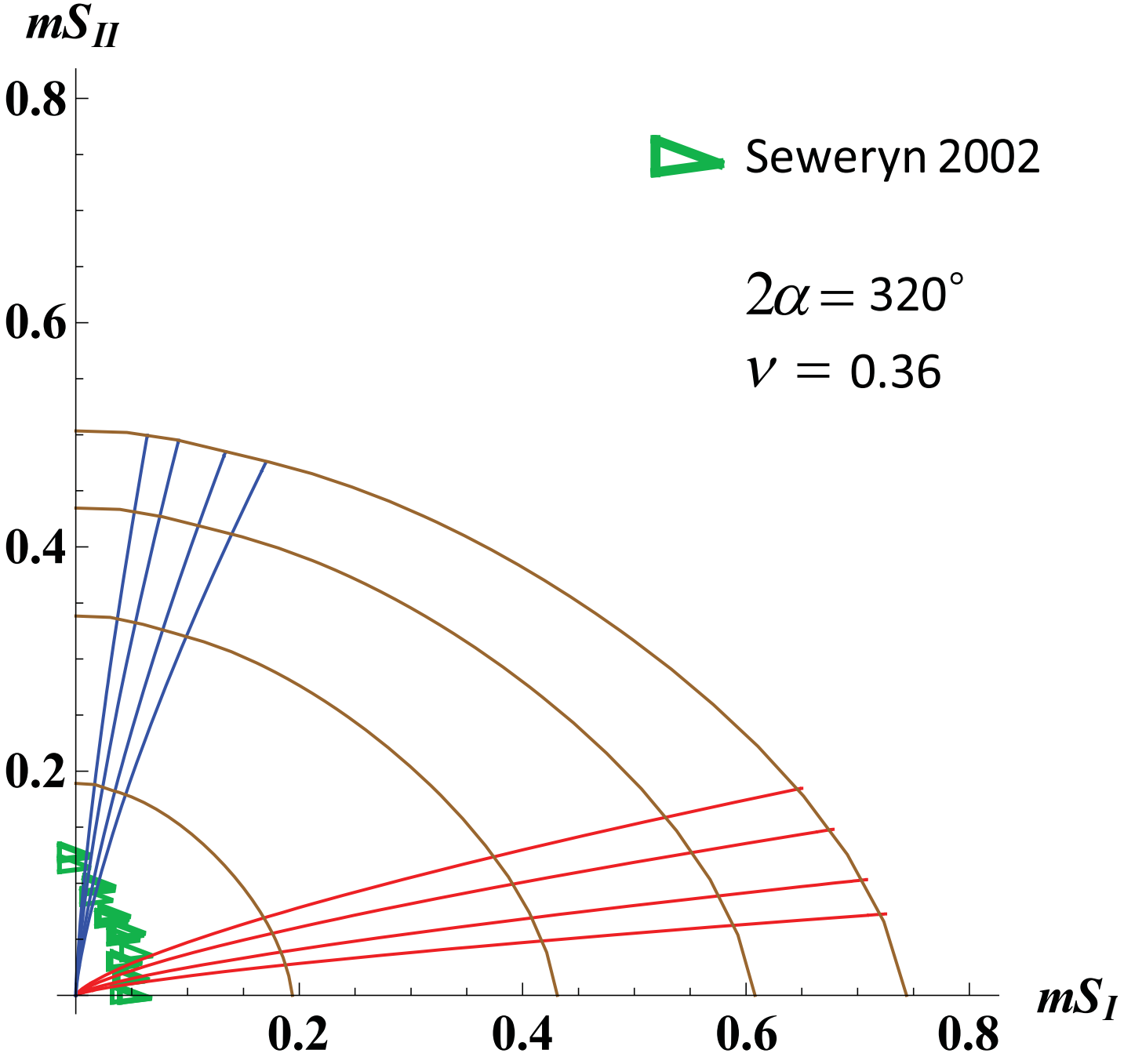
mS_{II}
0.8
0.6
0.4
0.2
Seweryn 2002
$2\alpha = 320^\circ$
$\nu = 0.36$
0.2
0.4
0.6
0.8
mS_I

Figure11g

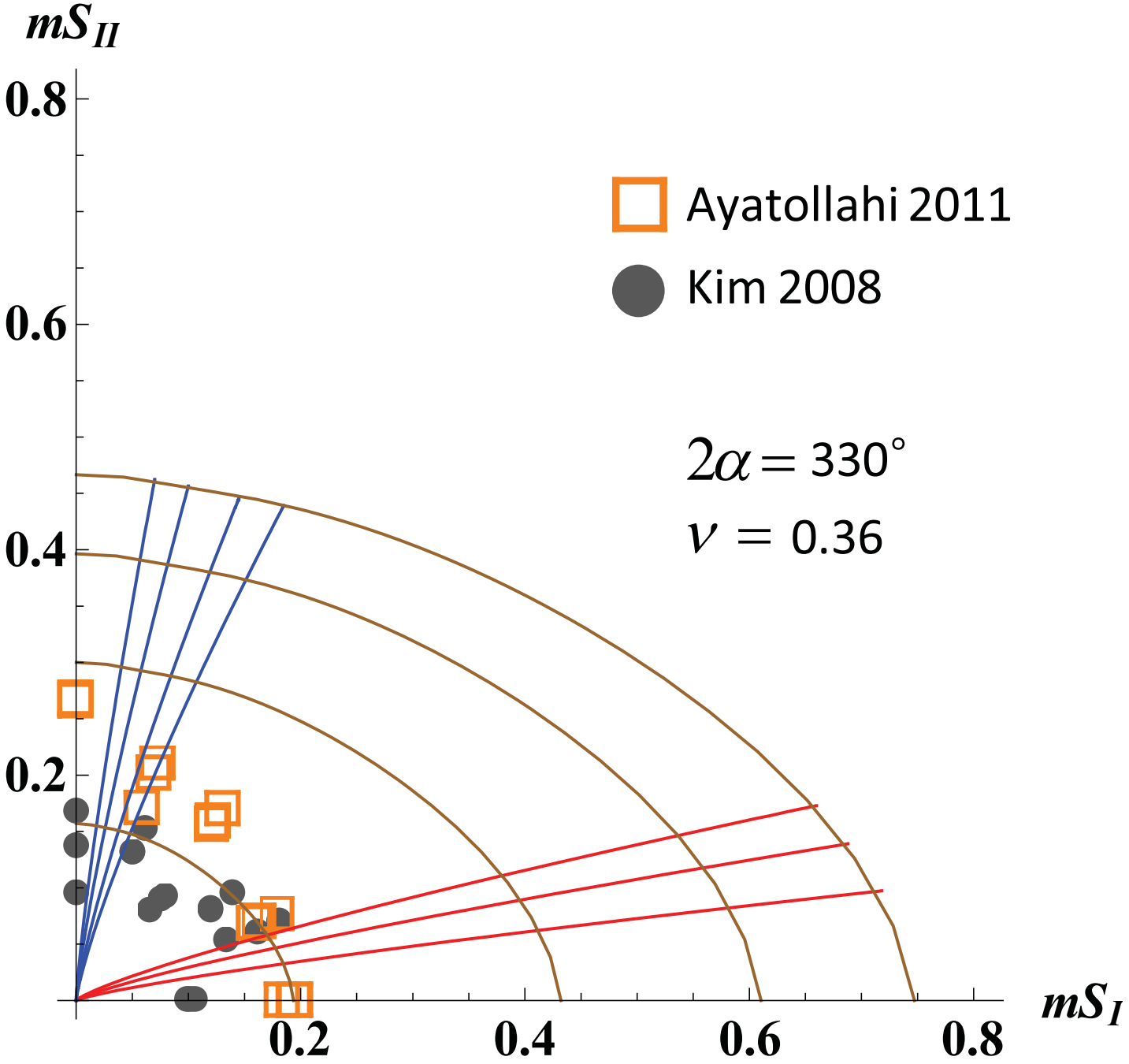
mS_{II}
0.8
0.6
0.4
0.2
0.2
0.4
0.6
0.8
mS_I
Ayatollahi 2011
Kim 2008
$2\alpha = 330^\circ$
$\nu = 0.36$

Figure12

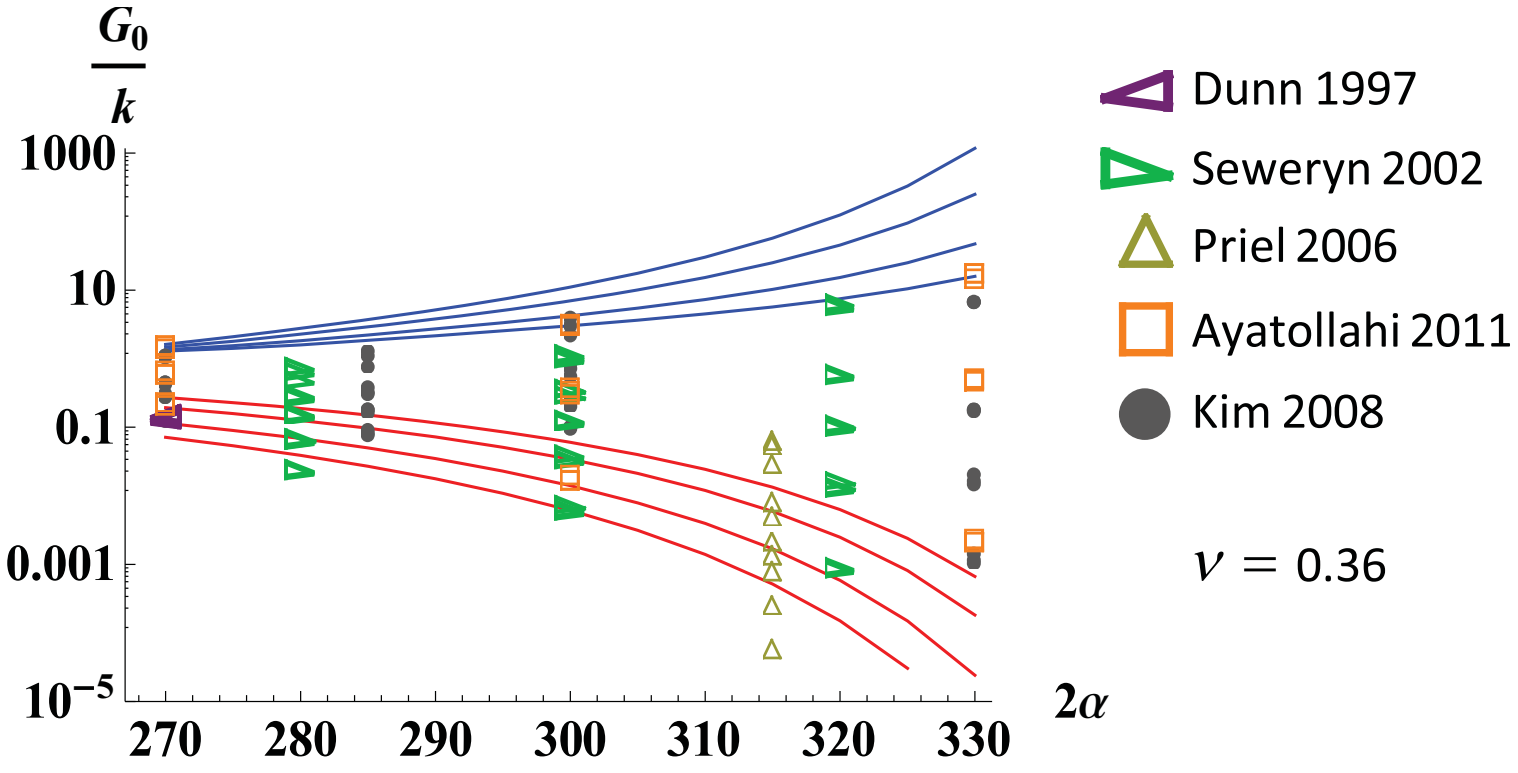
$\frac{G_0}{k}$
1000
10
0.1
0.001
10^{-5}
270
280
290
300
310
320
330
2α
Dunn 1997
Seweryn 2002
Priel 2006
Ayatollahi 2011
Kim 2008
$\nu = 0.36$

Figure13

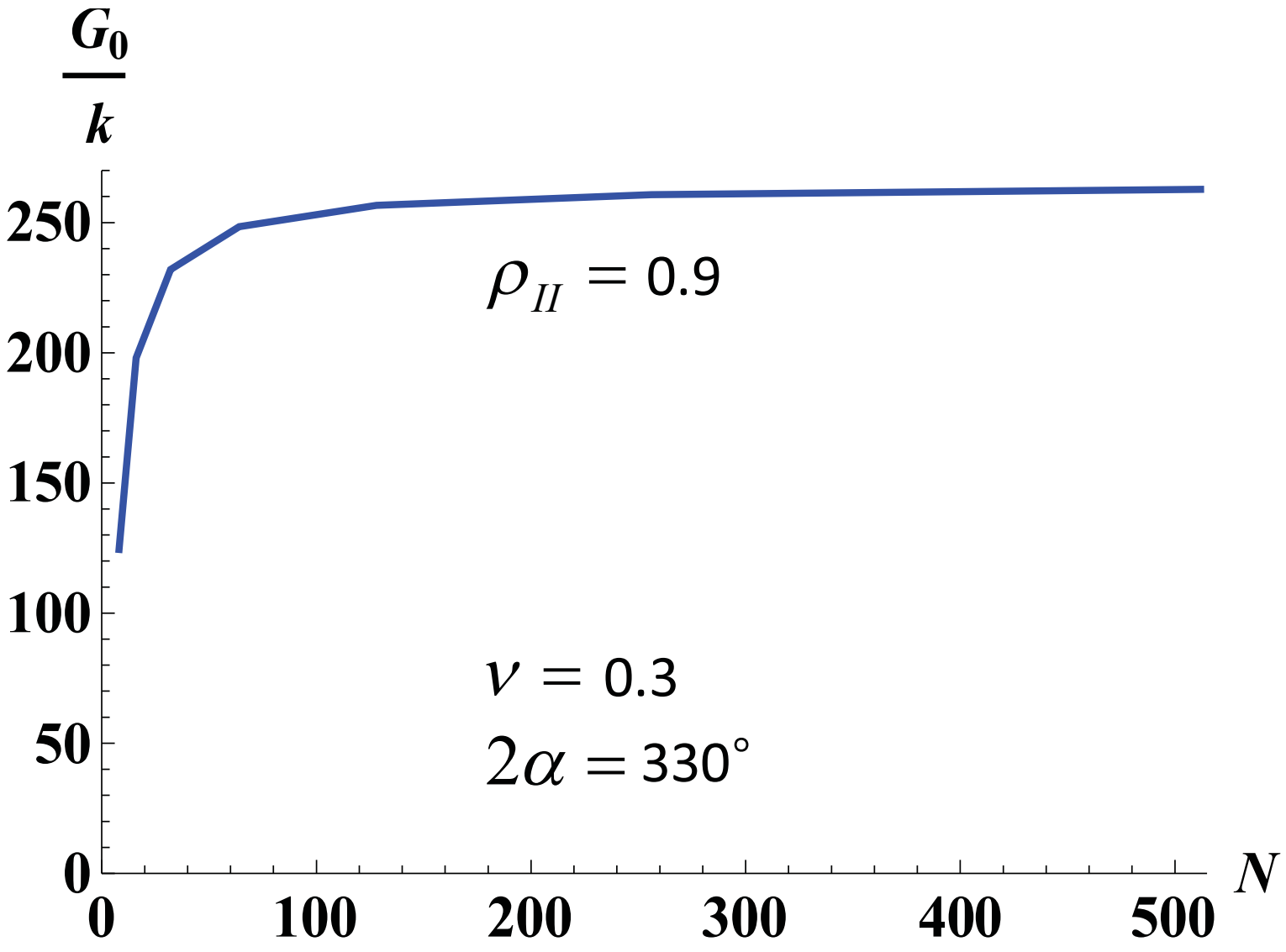
$\frac{G_0}{k}$
250
200
150
100
50
0
0
100
200
300
400
500
N
$\rho_{II} = 0.9$
$\nu = 0.3$
$2\alpha = 330^\circ$